Development of a Calorimeter for Clinical Proton Therapy Beams

Hiu Fung Wong

University College London

Submitted to University College London in fulfilment
of the requirements for the award of the
degree of Master of Philosophy.

October 17, 2017

Declaration

I, Hiu Fung Wong confirm that the work presented in this thesis is my own.
Where information has been derived from other sources,
I confirm that this has been indicated in the thesis.

Hiu Fung Wong (黃曉鳳)

Abstract

Proton therapy is a promising alternative to conventional X-ray radiotherapy in the treatment of cancer, particularly in regions at depth and close to critical structures. The conformity of proton therapy makes depth-dose calculations crucial, lest miscalculations lead to missing the target volume, especially at distal edges. X-ray computed tomography is used as a measure of absorption of photons through a patient for conventional radiotherapy, but the differing natures of photon and charged particle interaction can result in range calculation errors. Provided protons are of high enough energy to pass through the volume being imaged, it is possible to image the patient using protons rather than photons. This requires that the path and residual energy of the protons after passing through a volume can be determined with good resolution.

An optical module developed initially for the SuperNEMO calorimeter shows potential for clinical applications and is being adapted for use as a proton calorimeter. This report describes studies to characterise the energy resolution of these modules with a view to using them for proton-based 3D tomography.

This report describes studies to characterise the energy resolution of these modules with a view to using them for proton-based 3D tomography. Pulse-shape analysis and application of χ^2 filters were used with the aim of reducing pile-up events in recorded waveform data. While the fitting was successful, it did not result in a significantly improved energy resolution for any of the datasets investigated.

Acknowledgements

This piece of research wouldn't have been possible without the help and support of a whole host of people, for whom I am most grateful. First and foremost, I would like to say thank you to the entirety of the UCL HEP group for all their combined time, efforts, support, free sandwiches... It doesn't matter what level of academia you're at, there will always be The Stampede once notification goes out.

I would like to thank and extend my gratitude to my supervisor, Simon Jolly, for giving me this opportunity in the first place and for his undying willingness to help. Trying to sum all of this experience up would take more words and articulation of thoughts and feelings than I am capable of, so I'll just leave it there. For all her help, support (well above and beyond the call of duty!), patience, encouragement, and friendship, I'd like to thank Anastasia Basharina-Freshville — I 100% couldn't have done it without you. I'd also like to thank Ruben Saakyan for his advice, encouragement, and help (even going as far as to quite literally "write code" on paper). To my second supervisor, Gary Royle, for his clarity and insight, and his generosity. My thanks to Philip Litchfield for his help and incredible generosity.

My thanks also to the staff of Clatterbridge Cancer Centre, particularly Andrzej Kacperek for sharing his expertise of the facility and beamline, and also for his wit and humour.

My thanks to my friends, too many to name all individually but you know who you are. My fellow HEPers... In particular I'd like to thank Anastasia, Andy Bell, Laurie McClymont, Vincenzo Monachello, Ashwin Chopra, Stefan Richter, Maciej Pfutzner, Ricky Nathvani, Marco Montella, and Will Breaden Madden for my sanity and the caring periodic reminders to refuel, recaffeinate, and to go the [redacted] to sleep. 谢芳 (Fang Xie) for being one of the best friends one could ask for — if I could only choose one thing to be grateful for after everything, it'd be meeting you. Non-HEPers... Natalie Arnold, Stephanie Möschter, Mei-chan and Tara-chan, Elliot Harris, and Donna Nicholl for all your encouragement. Rita Howe, go raibh maith agat. You are wiser than salmon, and I am honoured to have you as a friend.

This whole endeavour was harder than I expected. It's taught me a lot of things, not only about physics or research, but life. So, above all, I want to thank my parents — this work is for you as much as it is for me. For my father, who instilled a love and curiosity of the universe in me at the very beginning. Who worked hard to provide for us, and who showed his love and care in his own quiet way. Thank you, father. I miss you. (And Black Jack - thank you for 18 wonderful years of companionship.) Most of all, for my mother. Dear Mammy, thank you for always being there for me. For all your advice. For your incredible support. For your care. For the (life) time you dedicated to raising me to the absolute best of your ability. For your love. You are the best and most selfless mother I could ever hope to have, and I am always thankful. This is for you. I love you. Thank you, for everything.

Contents

List of Figures

List of Tables

1 Introduction

Cancer is the collective name given to the class of diseases caused by the uncontrolled proliferation of the body's cells. This can result in tumours that are malignant, i.e. those that are prone to pathological invasion and spread. The ideal curative treatment is one in which the disease is completely eliminated from the body, with as few adverse effects as possible. The main approved modalities of cancer treatment—whether curative or palliative—are surgery, radiation therapy/radiotherapy (RT) and chemotherapy [17].

Due to the malignant nature of cancerous tumours, the disease may have spread further than can be seen on a clinical level and so success is greatly improved when more than one modality is combined (referred to as "multimodal therapy") [18]. In cases where surgery is unsuitable, radiotherapy often becomes the primary mode of treatment as a specific volume can be targeted and treated. This avoids some of the cellular subpopulation resistance-based recurrence/regrowth problems inherent with chemotherapy drugs, or immunotherapy agents that rely on assumed biological changes specific to cancer cells such as biological markers or changes in cell metabolism [19].

While initial investment and commissioning costs for radiotherapy are high [20], it comprises approximately 40% of all curative treatment [21, 22] while accounting for 5% of total care costs [23]. Charged particle radiotherapy using protons is an attractive form of treatment on account of the desirable physics properties of the particles when interacting with the attenuating matter. Treatment planning for proton therapy currently uses the same X-ray technology as used for conventional X-ray radiotherapy, despite differences in interaction mechanisms between photons and charged particles. This leads to some uncertainties in treatment planning, which could be improved with a proton-based imaging system.

As this project straddles both the medical physics and high-energy physics domains, this report contains an overview of aspects of both fields to provide the background and basis for proton computed tomography. Sections 2–5 describe the basics of radiotherapy, ionising radiation interactions with matter and proton computed tomography. Calorimeter details, experimental setup and recorded data are described in Sections 6–7. Analysis of obtained data and results are contained in Sections 7.1.1 onwards.

2 Radiotherapy

Radiotherapy can be split into two main types: external beam radiotherapy (EBRT) and internal. EBRT is the most common type and is termed thus as the ionising radiation is delivered from an external source outside the patient and directed at the treatment area. While the aim is to use ionising radiation for the purposes of cell killing and cancer cure, the mechanism for damage of cellular DNA does not discriminate between healthy cells and cancer cells and therefore treatment carries the hazardous risk of inducing carcinogenesis, the process by which normal cells are transformed into cancer cells [24]. It is ethically dubious therefore to propose a difficult or arduous course of treatment with the intention of curing a person [of cancer] if it carries with it a high risk of late treatment-induced mortality or severely reduced quality of life.

In medical physics, the energy deposited in matter by a monoenergetic ionising radiation beam is defined in terms of the mean energy $\bar{\varepsilon}$ imparted to a mass m and is referred to as the physical *absorbed dose*, D, where:

$$D = \frac{\mathrm{d}\bar{\varepsilon}}{\mathrm{d}m} \tag{1}$$

where the unit of absorbed dose is Joules per kilogram (Jkg^{-1}) and is known as a Gray (Gy).

A specific effect may occur at a given time after irradiation; this is referred to as an endpoint and may be a desirable outcome such as clonogenic (those which have the potential to proliferate) tumour cell death, or an adverse effect such as oedema or inflammation. In clinical practice a broad range of doses is observed where the chances of a specific radiation reaction or endpoint increases with increasing dose (i.e. a dose-response relationship). Curing cancer via radiotherapy requires the delivery of a specific predetermined dose calculated as necessary for the death of all clonogenic tumour cells to a predefined defined tumour volume. The ideal RT treatment plan is one that delivers a defined dose distribution within a target volume and none outside it [25]. Treatment plans are hence designed with the intention of delivering maximum target dose to the target volume with as minimal dose to the healthy tissue surrounding it as possible.

EBRT is presently most commonly carried out with high energy X-ray photons typically in the range 4–25 MeV, with choice of energy depending on depth of the tumour (see Fig. 2). Higher energies are preferred for tumours beneath the skin or deeper in the tissue, as the point of dose maximum is then deposited beneath the surface of the skin with more skin-sparing as a result [26]. To achieve uniform dose and to reduce levels delivered to healthy tissue, EBRT is usually carried out with beams from multiple directions.

Pre-treatment patient imaging is required for the purposes of visualisation and treatment planning (see section 5). Once a patient has been imaged, there exists a

difference between the actual patient and the virtual patient upon which the treatment planning is performed. Effective patient immobilisation, e.g. via immobilisation shells and masks, is required to reduce positioning errors by recreating as much as possible the positioning of the patient at imaging during treatment and thus must be compatible and oriented the same in both systems. The radiation isocentre is the point in space where the radiation beams intersect when the gantry is rotated. The gantry of the linear accelerator treatment beams rotate about the isocentre to deliver dose to the Treatment Volume centred at that point [27]. Rotation of the treatment beam allows for beams to be delivered at multiple angles to limit dose to healthy tissue and organs at risk.

Definition of a specific target volume is necessary for 3D treatment planning, the guidance and delivery of said plan and dose reporting for comparison of actual irradiated volume versus target volume and evaluation of outcomes. Volume specifications with different definitions, as outlined by International Commission on Radiation Units and Measurements (ICRU) Reports No. 50 and 62 [28, 29], are used to define the various target volumes and how they relate to each other. Fig. 1 indicates the various treatment volumes, from the Gross Tumour Volume (GTV) that is actually visible on the planning CT, all the way out to the Planning Target Volume (PTV) that is the targeted area for irradiation. The intermediate volumes represent the additions of the various margins of error required to account for uncertainties in both the volume being treated due to patient alignment and also the full extent of the tumour.

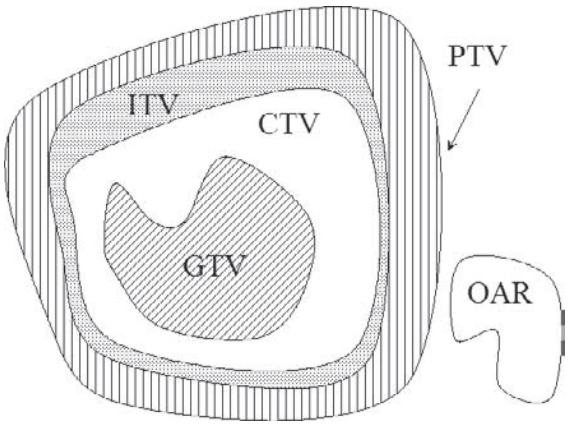

Figure 1: *Volumes of interest as defined in ICRU Reports No. 50 and 62 [1]. GTV = Gross Tumour Volume. CTV = Clinical Target Volume. ITV = Internal Target Volume. PTV = Planning Target Volume. OAR = organ at risk.*

Limitations of treatment techniques and case-by-case variations means the volume receiving the prescribed dose level required for the purpose of treatment may not accurately conform to the PTV and may be larger. The actual tissue volume that is planned to receive the required dose level is called the Treated Volume (TrV), with the Irradiated Volume (IrV) being the tissue volume receiving a dose considered significant in relation to normal tissue tolerance, which varies depending on the tissue [30]. The TrV is bordered by the isodose surface for the minimum target dose for treatment (e.g. 95% of the prescribed dose) such that the entirety of all target volumes shown in Figure 1 will receive the minimum target dose. However, this can

mean the actual IrV may extend to healthy tissues and close to OAR. Beam shaping and conformal radiotherapy aims to reduce both the TrV and IrV [28].

3 Hadron Therapy

Hadron therapy is a form of charged particle EBRT utilising hadrons in place of photons to treat the defined target volume. All existing hadron therapy treatment facilities use either protons or Carbon-12 ions, with the vast majority using protons [31].

Due to the shape of the energy-loss curve, the depth-dose distribution of heavy charged particles displays an increasing energy deposition with penetration distance, culminating in a maximum at the end of the range followed by a sharp distal drop-off as it runs out of energy: this is shown in Fig. 2. These are referred to respectively as the "Bragg curve" and "Bragg peak" [32, 33], the range of which is proportional to the energy of the charged particle and can be predicted by the Bethe equation (see Section 4.2).

These properties of protons and heavier charged particles to display a finite range, greater peak-to-entrance dose ratio and maximum energy deposition towards the end of the curve have long been considered highly promising for therapeutic purposes [34] with the tissue-sparing potential enabling delivery of more conformal doses to the tumour [35]. Both proton and ion therapy have been of increasing interest especially in recent decades, as associated technology becomes more advanced and more facilities purpose-built for clinical settings have been constructed [36].[1]

Despite the sharper Bragg peak, more rapid distal fall off and increased ratio between entrance dose to maximum peak dose, the use of heavier ions causes a tail at depths beyond the Bragg peak due to nuclear fragmentation of the incident beam. The length of this tail beyond the Bragg peak extends as a function of energy (see Carbon ion curves in Fig. 2). For sensitive or critical structures where it is important that as little dose as possible is delivered to healthy tissue beyond that of the target volume—such as the optic nerve behind the retina to preserve vision—protons are often preferred [37].

Uniform dose delivery over the desired target volume requires a superposition of so-called "pristine" Bragg peaks with carefully selected intensities and energies. The distributions are spread out in depth and thus termed "spread-out Bragg peaks" (SOBPs): this is shown in Fig. 3. While entrance dose is increased significantly due to the additional shallower peaks, it is still less than the high initial entrance dose deposited by photon beams of equivalent dose at the same depth (the photon and proton beams in Fig. 2 display the same entrance doses, however the photons display markedly reduced dose at the target depth). The highly conformal dose regions allow

[1] In contrast to the initial use of research facilities offering treatment as an adjunct purpose.

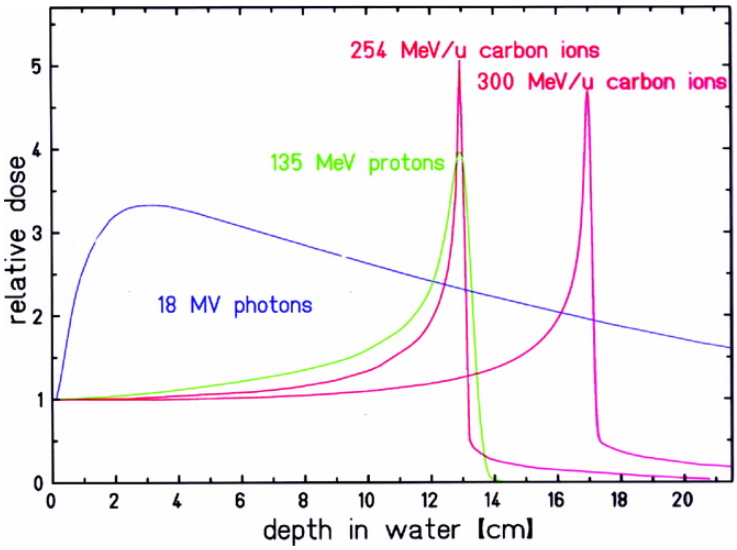

Figure 2: *Comparison depth-dose profiles of radiotherapy beams with 18 MeV photons (blue), 135 MeV protons (green) and 254 and 300 MeV/u carbon ions (red and magenta) [2].)*

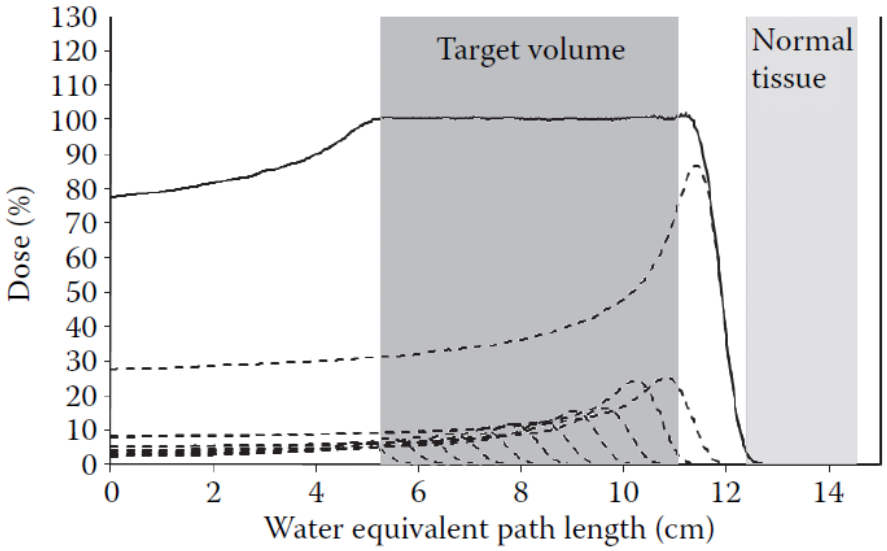

Figure 3: *SOBP construction: Solid line = SOBP depth-dose distribution, dashed lines = component Bragg peaks [3].*

for the potential of high accuracy of target volume coverage and reduction of integral dose to healthy tissue.

Despite this tighter dose conformality that is clearly possible with protons over conventional X-ray radiotherapy, extra margins need to be introduced when treating with protons that mitigate some of this advantage due to the imaging modality used when defining the various treatment volumes (see Section 2). Imaging for treatment planning is carried out almost exclusively with X-ray CT, which one then has to convert to the appropriate proton absorption: this is dealt with in more detail in Section 5. To take into account the conversion errors introduced when an X-ray CT scan is converted into a format to be used for proton treatment plans, the treatment plan includes within it a margin of error specifically for the uncertainty in this conversion. As the conversion error arises from differences in matter interaction between X-ray photons and protons, imaging with the same type of particle as for treatment — in this case protons — should reduce or eliminate the conversion error margin, thus shrinking the PTV and sparing healthy tissue that would otherwise be irradiated.

4 Ionising Radiation Interactions

The biological effects of ionising radiation can be divided into two types, depending on the type of radiation: directly ionising (charged particles) and indirectly ionising (photons and uncharged particles).

4.1 Photon Interactions

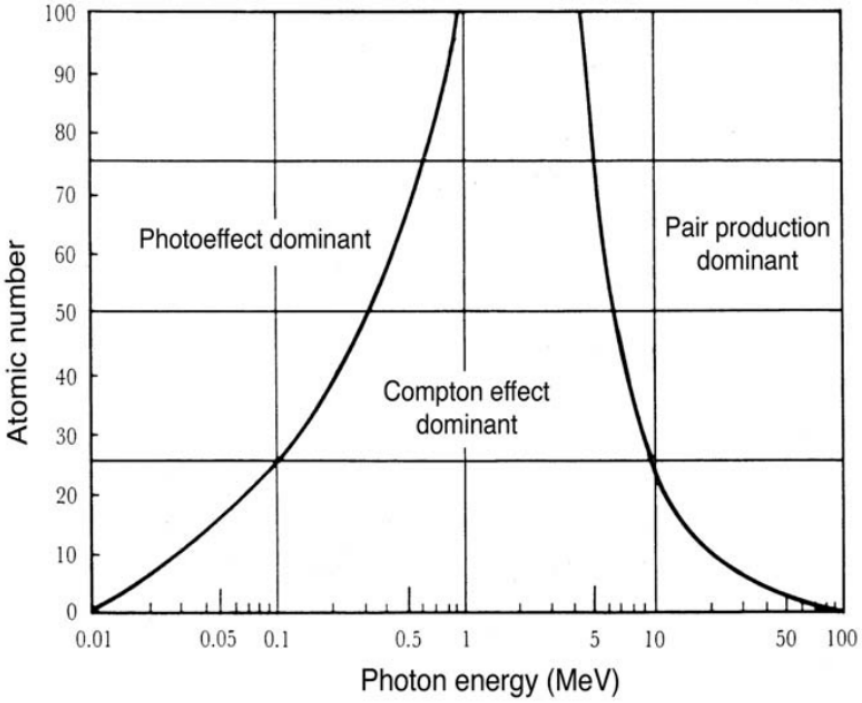

Figure 4: *Regions of relative predominance of the three main forms of photon-matter interactions [4]. For Carbon $Z = 6$, Oxygen $Z = 8$, Hydrogen $Z = 1$.*

Conventional radiotherapy uses external beams of photons as the ionising radiation for cell killing. For an attenuating material or absorber at depth x with elemental thickness $\mathrm{d}x$, the probability of a photon-absorbing event occurring is proportional to the number of photons available, N, at that particular point which has n atoms per unit volume is:

$$-\mathrm{d}N = \sigma_{\mathrm{tot}} N n \, \mathrm{d}x \tag{2}$$

where σ_{tot} is the cross-section of interaction and is highly dependant upon the material. The human body is composed mainly of carbon, oxygen and hydrogen; proportions vary with tissue type. If n and σ_{tot} are constant with regards to x for one

tissue type, integration over the full depth x is:

$$-\int_{N(0)}^{N} \frac{\mathrm{d}N}{N} = \sigma_{\mathrm{tot}} n \int_{0}^{x} \mathrm{d}x \tag{3}$$

$$N = N(0)\mathrm{e}^{-\sigma_{\mathrm{tot}} n x} \tag{4}$$

where $N(0)$ and $N(x)$ are the number of photons before and after attenuation, respectively. The Intensity I, defined as the number of photons per second, therefore falls off exponentially with depth, with the intensity $I(x)$ at depth x given by:

$$I(x) = I(0)e^{-\mu(h\nu,Z)x} \tag{5}$$

The product $-\sigma_{\mathrm{tot}} n$ has been replaced with the *linear attenuation coefficient*, μ (cm^{-1}), which expresses interaction probability for photons of a particular energy per unit length for a given material [38] (e.g. 0.02219, 0.0230, and 0.0444 cm^{-1} for 1 MeV photons in water, muscle and bone respectively [39]). The nature of the photon interaction with the attenuating matter depends largely on the energy of the incoming photon ($h\nu$) and the atomic number (Z) of the atoms in the attenuator (Fig. 4).

The photon interaction may be with a tightly bound orbital electron: the complete absorption of the photon results in the ejection of a photo-electron (photoelectric effect). The photon may also interact with an essentially free electron, resulting in some loss of energy of the photon and recoil of the electron (Compton effect). The photon can also interact with the nuclear field of a nucleus, resulting in a production of an electron-positron pair (pair-production).

Photons are considered an indirectly ionising form of radiation; they are uncharged and thus deposit energy in the medium via a two-step process:

1. For the MeV-range photons used in radiotherapy, energy is first transferred to the kinetic energy of atomic electrons predominantly by Compton scattering, with a small contribution at low energies from the photoelectric effect (see Fig. 4). At these energies, the contribution from pair production is small. Photons themselves, however, are not directly capable of producing multiple ionisation events characterised by charged particle interactions.

2. The liberated electrons then impart energy to the medium through direct Coulomb interactions with other orbital electrons. Given enough energy, these orbital electrons may be ionised and go on to further liberate other orbital electrons, resulting in an electron cascade. Most biological damage is inflicted by these liberated electrons as opposed to the primary photon interactions [40, 1].

An important point to recognise is that the location where the dose is deposited is not where an X-ray photon first interacts with an atom within the medium, but where the energy of the charged particle it liberated is absorbed. This results in the build-up region seen in the first 2 cm of the photon curve in Fig. 2.

4.2 Charged Particle Interactions

The charged particles used in charged particle EBRT travel through matter and interact Coulombicly with atomic orbital electrons and nuclei. Interactions may be elastic or inelastic in nature and can result in a change in the particle's direction or a loss in its kinetic energy.

Charged particles are considered a directly ionising form of radiation, as they can deposit energy in the medium via a direct one-step process with atomic electrons. Interactions are generally divided into collisional and radiative (nuclear field) interactions. Collisional interactions result from charged particle interactions with orbital electrons and lead to atomic excitations and ionisations. At the energies relevant for clinical medical physics these are the main means by which charged particles deposit their energy in matter. Nuclear field interactions with atomic nuclei can be elastic collisions which may change the trajectory of the incident charged particle, or inelastic collisions which result in the production of a photon and energy loss from the incident charged particle. A subset of inelastic processes involves the radiation of a photon due to conservation of momentum from the deceleration or deflection of the charged particle as it passes through the nuclear Coulomb field: this is called Bremsstrahlung radiation.

The angular deflection of an incident charged particle as it traverses an absorber is a statistical outcome of many interactions and resulting deflections [3]. It is described by the statistical theory of Multiple Coulomb Scattering (MCS) [41, 42]. For a material of such thickness that the number of interactions becomes high, the central limit theorem applies where given a large enough sample size, the mean angular dispersion of many small displacements can be modelled as Gaussian (Equation 6) [43]. The angular dispersion θ_0 can be given by:

$$\theta_0 = \frac{13.6MeV}{\beta cp} z \sqrt{\frac{x}{X_0}} \left[1 + 0.038 ln \left(\frac{x}{X_0} \right) \right] \tag{6}$$

where p, c, and z are the momentum, velocity, and charge number of the incident particle, and x/X_0 is the thickness of the scattering medium in radiation lengths, a quality characteristic of the material and can be found tabulated [44] or calculated via an approximation [45]. This is important when considering image reconstruction purposes as the deviation of a particle needs to be known if the track of the particle through the medium it has passed through is to be reconstructed.

Stopping power (dE/dx) is the retarding force acting on charged particles due to interactions with matter. The energy loss of charged particles that are not highly relativistic is described by the Bethe equation [33, 46]:

$$-\left\langle \frac{\mathrm{d}E}{\mathrm{d}x} \right\rangle = kz^2 \frac{Z}{A} \frac{1}{\beta^2} \left[\frac{1}{2} \ln \frac{2m_e c^2 \beta^2 \gamma^2 T_{\max}}{I^2} - \beta^2 - \frac{\delta(\beta\gamma)}{2} \right] \tag{7}$$

where Z and A are the atomic number and atomic mass of the absorber, z is the charge of the incident particle, $I \simeq 11.5Z\,\mathrm{eV}$ is the mean ionisation potential, $T_{max} =$

$2m_e c^2\beta^2\gamma^2/[1 + 2\gamma m_e/M + (m_e/M)^2]$ is the maximum kinetic energy that may be imparted to an electron in a single collision, $k = 4\pi N_A r_e^2 m_e c^2$, and β and γ are the conventional relativistic factors. $\delta(\beta\gamma)$ is the Fermi density correction term for ionisation energy loss caused by target material polarisation [47].

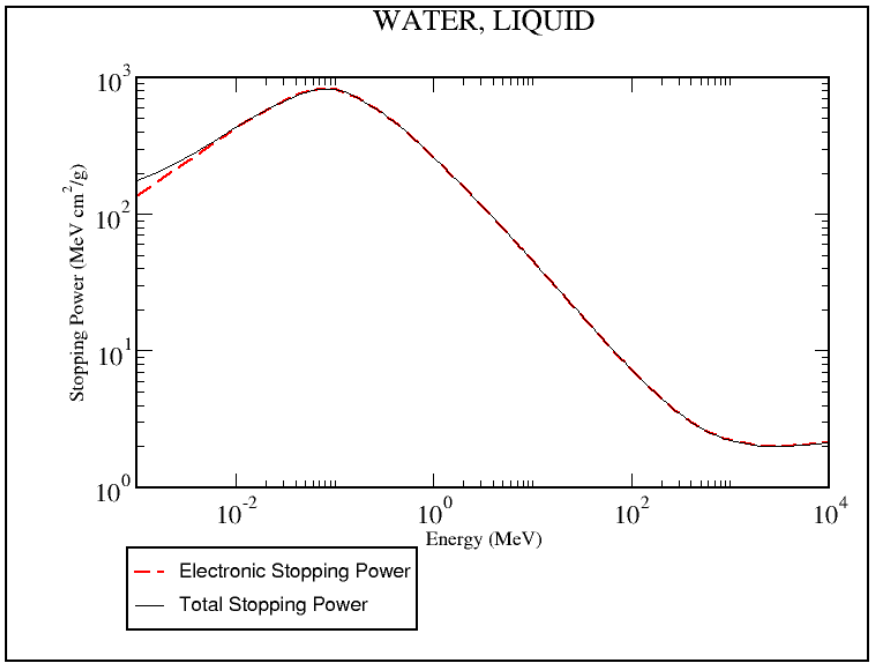

Figure 5: *Stopping power for protons in water as a function of kinetic energy [5].*

The probability of a nuclear interaction resulting in a significant fraction of energy loss is much smaller than that of collisional losses. For protons travelling through water, the stopping power as a function of energy is shown in Fig. 5. Past the maximum, stopping power decreases roughly as the inverse-squared of the increasing particle velocity before rising again at higher energies. A particle with mean energy loss rate through matter close to the minimum is referred to as "minimum ionising". dE/dx increases rapidly as the particle loses energy, resulting in increased energy deposition, particularly towards the end of the particle track. This results in the characteristic Bragg peak of energy deposition in heavy charged particle interactions (see Fig. 2).

5 Proton Computed Tomography

To deliver a specific dose to a defined volume within a patient, a treatment plan must be developed in three dimensions. A 3D treatment plan requires a 3D representation/map of the patient. This is usually obtained via X-ray computed tomography (XRCT), as it is faster and less expensive—and thus more common—when compared to magnetic resonance imaging (MRI) despite the latter's superior soft-tissue imaging capabilities [48]. During an XRCT scan, X-ray projections from a large number of orientations around the body in one plane are recorded as a detector-source array rotates around the body, measuring a slice of the area of the body under investigation. Once a full rotation has been completed, the array moves to a new plane in the body and another slice is recorded. While a variety of mathematical techniques exist for the conversion of these many X-ray projections at the various angles obtained into cross-sectional images of the body, filtered backprojection (FBP) is one of the more fast, simple and robust [49].

In FBP (illustrated in Fig. 6), detectors first record a forward projection of the X-ray intensity transmitted through that body section. A single forward projection is all the X-ray absorptions summed up along that line of projection. Once all forward projections for one rotation have been measured, the forward-projected value is back-projected along the ray path from each detector to each pixel on that path. Each region of overlap from all the combined back projections is assigned an absorption value based on the sum of the absorptions from each detector position, with the final backprojected image taken as the sum of all backprojected views. Back projection of the same value back along every pixel in the ray path results in a blurry backprojected image. To counteract this, each view is filtered via convolution with a 1D filter prior to backprojection to provide the reconstructed image [6]. One filter that can be used is the ramp filter, a high-pass filter enhancing the edges of an image where the signal changes most rapidly and eliminating low frequency signal that causes blurring of the reconstructed image.

X-ray attenuation is represented by a quantity called the CT number (Equation 8), measured in Hounsfield Units (HU). Images taken with a CT scanner are based on the passage of X-rays through the body and their amount of attenuation from both absorption and scatter; CT numbers are the equivalent of the per-mille difference between the linear attenuation coefficient μ (see Equation 5) of a voxel and that of water:

$$\text{CT number} = \frac{\mu_{\text{tissue}} - \mu_{\text{water}}}{\mu_{\text{water}}} \times 1000 \tag{8}$$

Examples of common substances in human body composition are: water = 0, air = -1000, fat = -100 to -50, muscle = 10 to 40, bone = 700 to 3000.

Protons are charged particles and their spread and depth of penetration are affected instead by MCS deflection and the stopping power (highly influenced by the

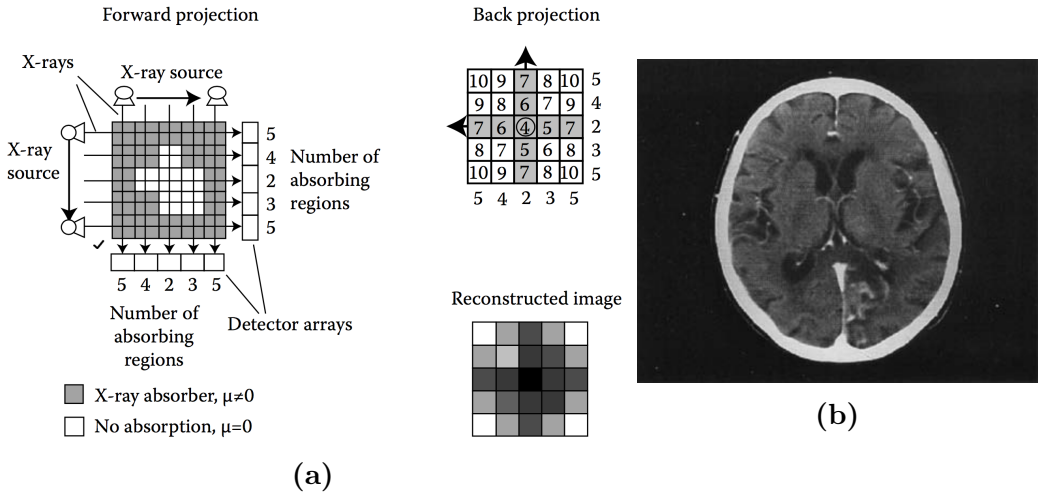

Figure 6: *FBP CT image reconstruction* ***(a)*** *for 2 source and detector orientations. The scanned tissue is represented by a greyscale indicating its absorption coefficient,* ***(b)*** *of cross-sectional image of the brain [6].*

electron density) of the absorbing material. Dose distributions for 3D treatment planning require conversion of CT number to relative stopping power via a calibration curve/graph (see Fig. 7): current treatment planning schemes/systems assume the X-ray attenuation coefficient to be proportional to electron density [50]. This introduces a conversion error when determining stopping power which then carries forward into an uncertainty on the evaluation of the proton range and is thought to contribute up to 1.8% of the total proton beam range uncertainty [51], where the total estimated uncertainties for treatment planning due to CT numbers and stopping powers are accounted for in clinical practice by a margin of 3.5% at both proximal and distal ends of the target volume [52].

For the photon beam, though healthy tissue is irradiated, the shallower dose fall-off means errors of depth-dose distribution at the lateral target volume is limited to a few percent. Conversely, while a photon beam still deposits dose past the target volume, proton dose deposition drops off sharply, as shown in Fig. 8. Although this is desirable for sparing healthy tissue as outlined in Section 3, errors or uncertainties in range (from setup errors, tissue inhomogeneities, patient motion, etc.) with a proton SOBP can mean the Bragg peak misses the distal portion of the target volume entirely, resulting in tumour recurrence.

The concept of proton CT (pCT) as a diagnostic imaging alternative is to reconstruct the electron density map using clinical proton beams and thereby provide a better estimate of proton stopping power and dose distribution during proton treatment planning. The use of the same proton beam as used for treatment would mean the patient would be in the same position as for treatment and provide a further decrease to error from patient setup. Protons with high enough energy to pass through

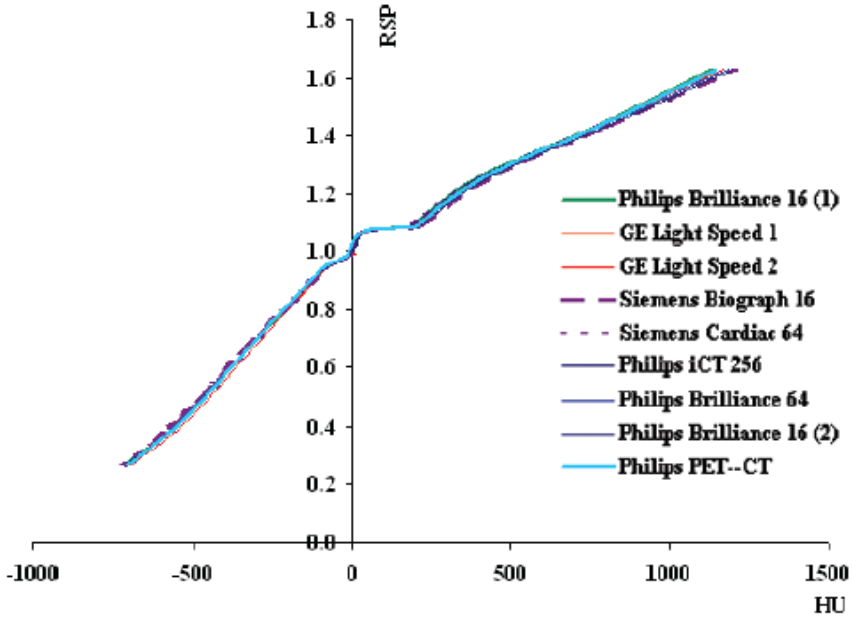

Figure 7: *Comparison of HU to relative stopping power (RSP) curves for nine CT scanners obtained with the same phantom [7], where RSP is the ratio of the stopping power between a given material and a given standard material [8], in this case water (1.0).*

a patient will deposit the majority of their energy beyond the body, since the Bragg peak falls outside the body. As such, since photons deposit the majority of their dose within the body, the use of protons for imaging could also potentially deliver a 3–5-fold lower dose to the patient than XRCT [53]. For pCT imaging, high-energy protons, ideally above 300 MeV, are used such that the Bragg peak falls on the far side of the patient and the particles may be detected on the other side and not stopped within the body.

Knowledge of two factors in particular are required for pCT image reconstruction: the path of the individual protons through the patient and the energy loss of said protons. As a starting point, most pCT reconstructions until recently have been based on the principles of FBP, with the CT number being replaced by stopping power (electron density) of the body's tissue and the proton energy loss allowing for the calculation of the stopping power. The assumption was also made that the geometrical path of protons through the image space was a straight line. While good density contrast has been found with pCT utilising FBP, spatial resolution is poor due to MCS, which makes the straight-line approximation inaccurate [54, 55, 56]. The proton path requires a spatial tracking system for individual events, as illustrated by Fig. 9.

An existing prototype of such a system under development by a group at Loma Linda University uses silicon strip tracker planes placed either side of the patient to

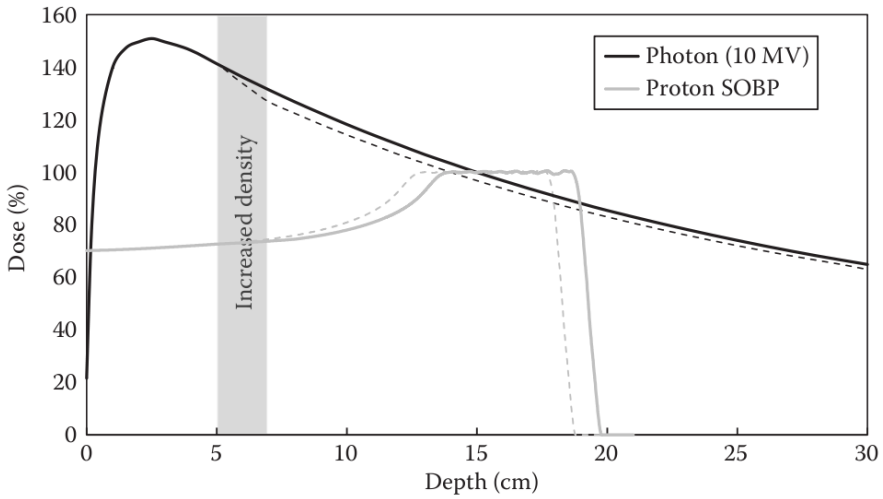

Figure 8: *Percent depth-dose (PDD) curve for 10-MV photon beam and proton SOBP. Dashed lines = PDD curves for the scenario of an increased density of medium at a depth of 5–7 cm. [3].*

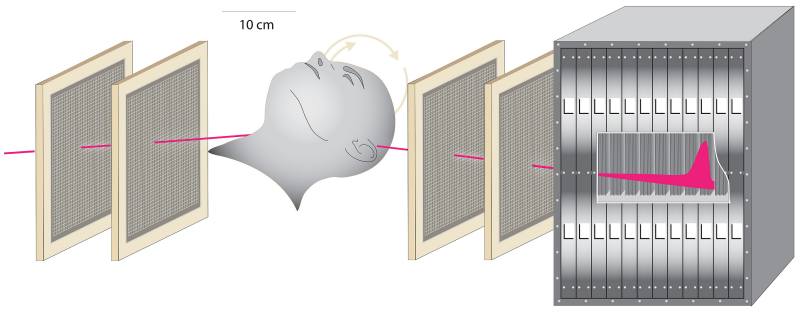

Figure 9: *Example of prototype pCT scanner. Protons pass through planes of fibres and the patient's head from the left. Residual energy or range after the patient is measured with a range telescope type calorimeter comprised of a stack of thin scintillator tiles (right) [9, 10].*

determine most likely proton paths, entry and exit points and direction [57]. Superior spatial resolution has been found to be achieved with a path of maximum likelihood taking MCS into account instead of a straight-line assumption, however computing MCS has proved to be a computer-intensive procedure [58]. More recent attempts have focused on combining FBP with an iterative projection algorithm, with the FBP as a starting point for the iterative procedure [49]. The energy loss of the proton traversing through the image object can be determined through knowledge of the proton's starting energy and its residual energy at the exit. As the most important parameter for determining density resolution in pCT, the energy loss measurement requires a separate calorimeter adapted for such events.

6 Calorimetry for Proton Computed Tomography

The number of protons required during data acquisition for meaningful reconstruction of a head-volume scan is on the order of 10^9 [53]. To complete the scan in a timeframe both reasonable in a clinical setting and for the patient (say $< 10\,\text{min.}$) a calorimeter should ideally be able to identify and collect events at a rate of at least 2 MHz. In addition, a calorimeter should ideally have an energy resolution less than that of the fluctuations in energy loss in a patient, which is typically on the order of $1\%\,\sigma$, close to the best achievable resolution for modern calorimeters [53].

6.1 Energy Resolution

Even a monoenergetic source will have a spread or distribution of energy (Gaussian or otherwise) in the detected particle energies, due to the inherent resolution of the detector. Measurement of a real source with a finite energy spread of its own ideally requires that a detector possess an energy resolution less than or equal to that of the beam spread to avoid convoluting measurements of the initial spread of energy values.

In the general case, the overall energy resolution dependance of a scintillation detector (σ_E/E) as the function of incoming radiation energy E can be summarised as the contributions of the stochastic fluctuations of deposited energy, A, the electronic noise of the photoreceiver, B and inhomogeneities/non-uniformities in hardware, calibration, scintillator light output, shower leakage[2], etc, C [59, 60]:

$$\frac{\sigma_E}{E} = \frac{A}{\sqrt{E}} \oplus \frac{B}{E} \oplus C \tag{9}$$

As the response of many detectors is approximately linear, it can be said that the number of particles reaching the sensor, N, is proportional to the amount of energy observed, therefore it can be written that $E = kN$ and $\sigma_E = k\sqrt{N}$, where k

[2]This may be alternatively described by a term $E^{-1/4}$ added in quadrature

is the gain of the system. For ideal (homogenous) calorimeters without leakage (i.e. where the shower is fully contained), the intrinsic energy resolution of a detector is dominated by the stochastic term, hence:

$$\frac{\sigma_E}{E} \propto \frac{\sigma_N}{N} \sim \frac{\sqrt{N}}{N} = \frac{1}{\sqrt{N}} \tag{10}$$

where E is the mean of the energy distribution.

For detectors in which deposited energy is measured via the light detected—most commonly scintillation detectors—energy resolution ($\Delta E/E$) is limited by the conversion of photons to an electrical signal, hence N is the number of photoelectrons generated [61]. The energy resolution can be expressed as:

$$\frac{\Delta E}{E} = \frac{2.35\sigma_E}{E} \tag{11}$$

where E is the mean of the full-width half maximum of the energy distribution ΔE. As a distribution may not be Gaussian, the full-width FWHM is more typically used instead of σ, to which it is related in the Gaussian case by a factor of $2\sqrt{2\ln 2}\sigma \approx 2.35\sigma$ [62, 63]. Energy resolution tends to improve with increased particle energy.

6.2 Energy & Range Straggling

For a monoenergetic beam travelling through a material of a given thickness that is less than the range of the particles, the beam will emerge with a spread of energies due to statistical fluctuations of the energy loss process. While MCS (Sec. 4.2) occurs within the material, the number of collisions and energy lost per collision is not constant and results in a broadened energy distribution curve of finite width known as the *energy straggling* peak. It is approximately Gaussian in shape, with its width increasing with the ratio Z/A, where Z is the atomic number and A the mass number, on account of reduced screening of inner electrons in elements of lower Z [64].

A related concept is that of *range straggling*. Identical charged particles, all possessing the same initial velocity or kinetic energy will not all have the same range. Stochastic variations in the rate of energy loss and number of collisions necessary to bring the particle to rest results not only in energy straggling, but in the observed ranges of individual particles from any monoenergetic source showing a Gaussian distribution about the mean range [65, 66].

6.3 Scintillation Mechanisms

Measurement of the amount of energy deposited from particles to matter can be achieved via the use of a material which releases a signal proportional to the energy

deposited. A scintillator is a material that exhibits luminescence when excited by ionising radiation—a process termed scintillation—making them particularly useful for the detection and spectroscopy of a wide range of radiation types [67]. There are two main types of scintillators: inorganic crystals and organic hydrocarbon-based compounds. While inorganics tend to have better light output and linearity, they are generally slow in response time in comparison to most organic scintillators, which tend to possess much better response times but lower light yields [68]. Since the detectors described in later sections make use of PolyVinyl Toluene and PolyStyrene organic bases, the following focusses on the scintillation mechanisms of organic scintillators.

Protons of 10–100 MeV will interact mainly with the orbital electrons of the atoms within the absorber as described by the processes in Section 4.2. Providing enough energy is transferred to the orbital electrons to result in ionisation, these electrons will then lose their kinetic energy via a combination of collisions of their own (which may then cause further ionisations), or via bremsstrahlung radiation. Should the bremsstrahlung photon energy be greater than 1.022 MeV — double the electron/positron rest mass — this can result in pair-production, the products of which can also go on to generate further cascades.

The process of fluorescence in organic scintillators comes from energy level transitions in individual molecules [61]. Interaction with incident radiation results in electronic excitations of molecules into discrete states. As the process is based on the energy level structure of a particular molecular species, fluorescence can be observed independent of state/phase [69]. Almost all organic plastic scintillators use polyvinyl-toluene (PVT) or polystyrene (PS) as a base, doped with a high concentration of "primary" fluorescent emitter (fluor) into the base—typically 1% by weight. A charged particle passing through the scintillator excites the base material, which rapidly transfers energy nonradiatively (Förster energy transfer) to molecules of the primary fluor, which is selected to re-irradiate at wavelengths more transparent to the base [11]. A secondary fluor, typically with 0.5% weight, absorbs the emitted UV from the primary fluor and re-radiates at a wavelength less attenuated by the PVT (Fig. 10). Both PVT and PS-based scintillators used for the calorimeter modules outlined in Section 6.4 and Section 8.1 are doped with para-terphenyl (pTP) as the primary fluor and 1,4-bis(5-phenyloxazol-2-yl) benzene (POPOP) as a secondary wavelength shifter. These are the most common dopants used for both base materials.

Plastic scintillators display non-linear response in light output and saturate at higher levels. As particles lose energy and the chances of interaction with the absorber increase, they become more densely ionising. For densely ionising particles, such as protons towards the end of their range, this can result in quenching of the primary excitation due to the lack of available energy states caused by the high density of ionised and excited molecules [70]. This can lead to non-linearity in amount of light given out in proportion to the energy deposited in the response of a detector.

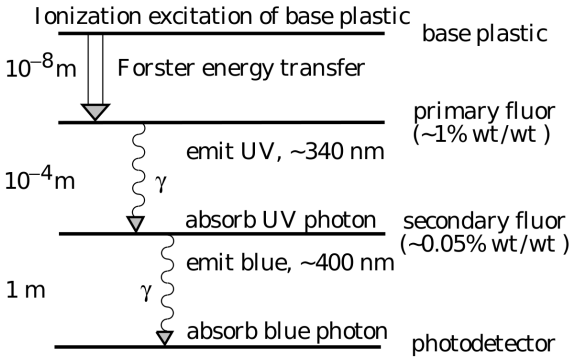

Figure 10: *Operating mechanism of plastic scintillator. Approximate fluor concentrations and energy transfer distances for the separate sub-processes shown [11].*

These effects are described by Birk's Law (Equation 12), which is given as:

$$\frac{dL}{dx} = S\frac{\frac{dE}{dx}}{1 + k_B\frac{dE}{dx}} \tag{12}$$

where L is the amount of light produced by a particle of energy E, $\frac{dE}{dx}$ the energy lost by the particle per unit track length, S is the scintillation efficiency and k_B is Birk's constant relating the density of ionisation to energy loss (typically on the order of 0.1 mm/MeV) [71].

6.4 SuperNEMO Calorimeter Module

An optical module developed during the R&D for the calorimeter of the SuperNEMO neutrinoless double beta decay experiment showed potential for clinical applications, as its organic plastic scintillator and high-QE (quantum efficiency) photocathode results in high and fast light output that is necessary for the large event rates required for operation in a high-throughput clinical environment. The calorimeter module consists of an 8-inch Hamamatsu photomultiplier tube (PMT) coupled using optical grease to an ELJEN EJ-200 hexagonal block of PVT, 276 mm in diameter and 193 mm deep and wrapped in 75 μm thick PFTE (Teflon) tape on the lateral sides and 12 μm thick mylar to increase light collection and uniformity. This calorimeter module will hereafter be referred to as the "Hex" module (Fig. 11). It has an energy resolution of 7.5% FWHM for 1 MeV electrons [72]. However, the detector is optimised for electrons of 0.5–4 MeV from double beta decay, whereas for pCT it shall be required for protons of energies greater than 100 MeV.

In medical physics, measurement of dose is usually calculated and calibrated as dose to water, since the human body is comprised of approximately 55–75% water [73] with an overall density close to 1 gcm^{-3}. This gives it similar absorption and scattering properties [74]. PVT has a proton stopping distance very similar to that

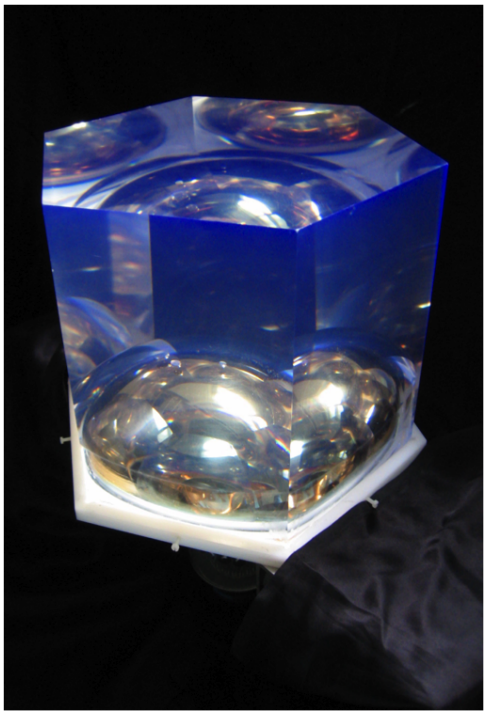

Figure 11: *Hexagonal PVT block of SuperNEMO optical module.*

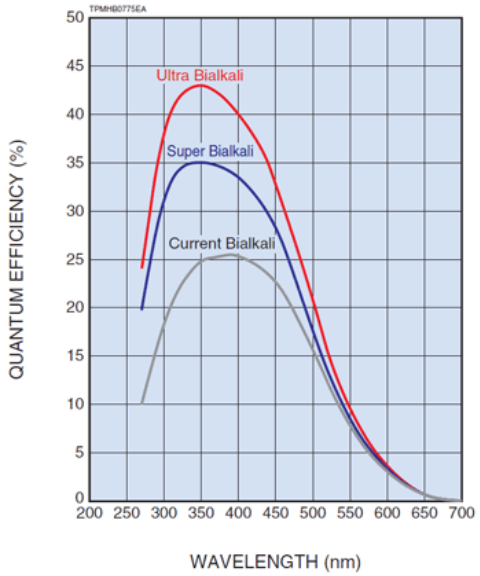

Figure 12: *Typical spectral response characteristics of a selection of Hamamatsu photocathodes [12]. The calorimeter photocathode uses the highest QE ultra bi-alkali.*

of water, making it useful for clinical dosimetry. At 60 MeV, the proton energy used for ocular cancer treatment, the range of protons is 30.93 mm in water and 30.02 mm in a vinyltoluene-based plastic scintillator [5].

The EJ-200 PVT block has a scintillation light yield of ∼10,000 photons/1 MeV e^- and a maximum wavelength emission of 425 nm as shown in Fig. 13. The Hamamatsu PMT photocathode is made of a bi-alkali Potassium-Caesium alloy from Hamamatsu's Ultra Bialkali range and has high quantum efficiency of >40% and a high sensitivity in the region close to 400 nm (Fig. 12, red line), making it a good match for the PVT scintillator [12]. The mylar reflective wrapping is thin and of low density to reduce energy loss as the particles pass through and its low Z minimises backscattering. The high reflectivity reflects photons that otherwise escape, improving the light collection efficiency of the detector.

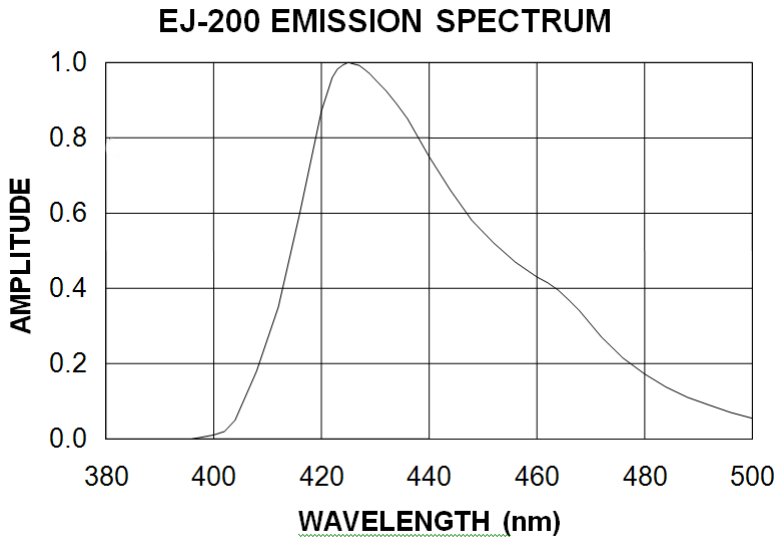

Figure 13: *Emission spectrum for ELJEN EJ-200 PVT plastic scintillator [13], used for the hexagonal block scintillator.*

7 Clatterbridge Cancer Centre

Characterisation of the energy resolution of the modules and investigation into recording of waveform data required data to be taken with an operational clinical proton beam. As the only operational proton beam therapy treatment centre in the UK at present, experimental testing has so far taken place at the National Centre for Eye Proton Therapy facility in the Clatterbridge Cancer Centre.

Housing the Douglas Cyclotron, the facility treatment beam line consists of a Scanditronix MC60PF isochronous cyclotron running at 25.7 MHz [75]. Hydrogen gas is ionised using a cold cathode discharge ion source [76]: the beam is extracted at 62 MeV along two straight sections of beam line with three sets of quadrupole triplets between the cyclotron and the treatment room.

The facility is capable of generating a 60 MeV clinical proton beam, which penetrates at maximum to a depth of 31 mm in water, with a distal fall-off of less than 1 mm. A selection of poly(methyl 2-methylpropenoate) (PMMA) modulators of varying thickness and range shifter wheels provide a uniform dose over the depth of the tumour during treatment (Fig. 14). PMMA is often used as a material for range shifting and a water-equivalent phantom material as it is dimensionally stable (the degree to which it maintains its original shape after exposure to stresses) and has a similar elemental composition and electron density to water [77]. The treatment beam (Fig. 15) has a flat beam profile [78] over an area of 34 mm in diameter without a collimator in the nozzle, or 30 mm in diameter with the largest size patient collimator in place [79]. Scattering foils are used to produce the flat beam profile; this, along with air absorption, is the cause of the energy drop from 62 MeV at extraction to the 60 MeV treatment beam [15].

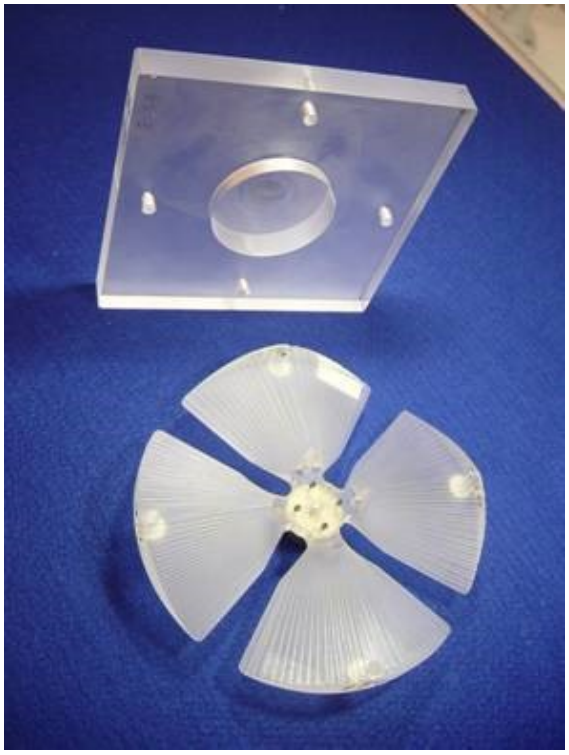

Figure 14: *PMMA modulator insert (top) and range shifter wheel (bottom) [14].*

During treatment, the beam is accelerated to the extraction energy and passes through two tungsten scattering foils with thicknesses of 0.017 mm and 0.027 mm set 300 mm apart. A brass stopper 6 mm in diameter and 7 mm thick set just before the centre of the second foil removes the core of the first scattered beam, exposing

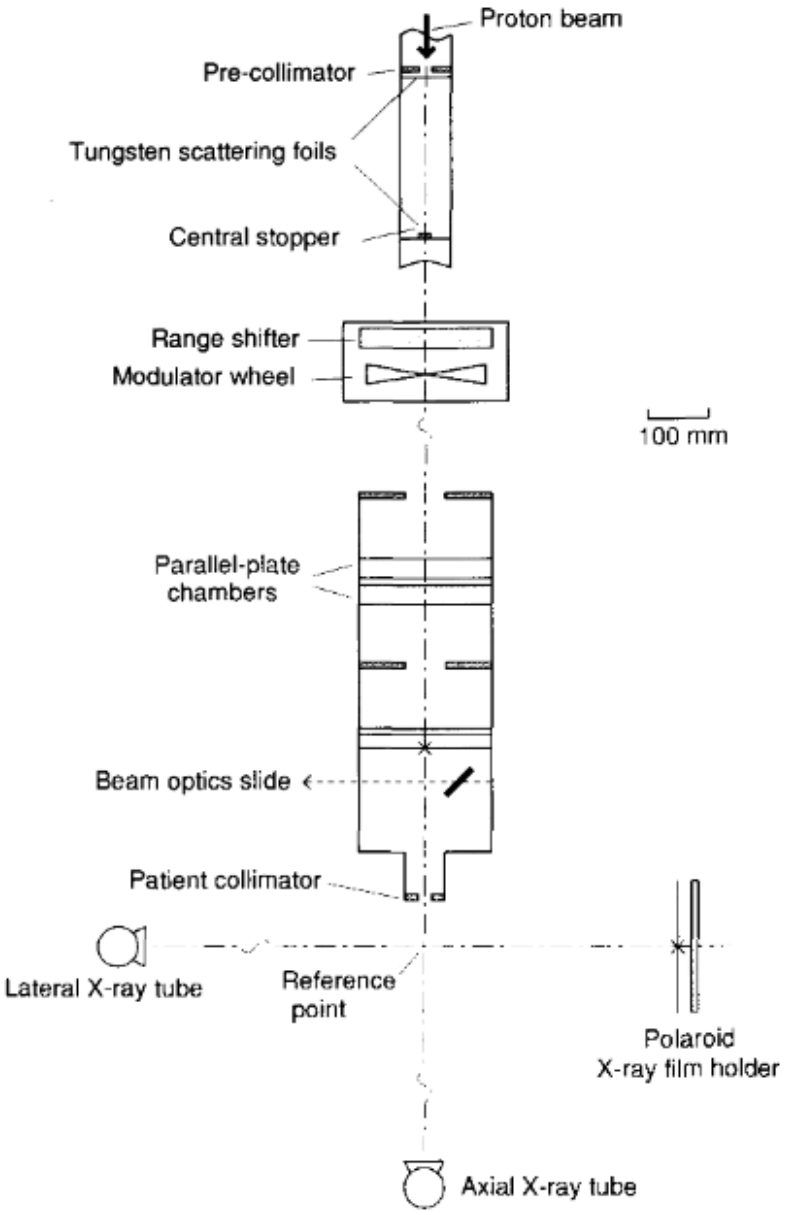

Figure 15: *Diagram of the beamline arrangement for proton therapy at Clatterbridge [15].*

the second foil to only a portion of the initially scattered beam, creating the flat distribution [80]. The beam then passes through a PMMA modulator and range shifter wheel set about 1 m upstream of the nozzle (Fig. 15) to modify the depth to which the protons reach and to generate a SOBP as mentioned in Section 3. Finally, brass collimators of either custom-cut shapes or varying circular diameters may be inserted into nozzle to shape the beam to the target area or desired size.

The first test beam run at Clatterbridge to evaluate the performance of the SuperNEMO Optical Module in response to 60 MeV protons took place on 8^{th} and 9^{th} July 2015. The Hex module calorimeter, within a light-tight box, was placed on a raised supporting wooden surface, secured to the patient treatment chair (Fig. 16). Alignment of the beam position to the centre of the module was guided by a field light, but approximate based on visual judgement. The field light consists of a high brightness LED, housed on a vertical slider within the treatment beamline casing, with a mirror that is capable of sliding into the beam axis (see "beam optics slide" in Fig. 15). The good photocathode uniformity possessed by the calorimeter across the entire surface of the PMT meant that precise centring of the proton beam was not critical. The calorimeter was connected via a patch panel to a HV supply for the necessary 800 V to operate the PMT and was alternately switched between being connected to an oscilloscope for the purposes of checking proton rates and rise times and a CAEN DT5751 digitiser for data recording. The CAEN digitiser has a 10-bit resolution with a sampling rate of 1 GS/s and is controlled by proprietary software on a Windows or Linux PC.

During acquisition of waveform data the timestamp (ns) and ADC input voltage (mV) are recorded along with the baseline signal level (mV). The proton beam is usually operated in a "treatment mode" for no longer than several minutes at a time for patient treatment: this limits the maximum treatment time and dose to ensure patient safety. For data collection, the beam was set to "physics mode" to disable maximum treatment time and dose monitor unit limitations and allow operation at a higher duty factor than for clinical treatment. Proton rates from the beam could be controlled to some extent via adjustment of the ion source gas supply and arc current, but obtaining a stable rate proved to be a challenge. Desired rates were achieved instead by attempting to find stable operating conditions at rates above the capability of the detector, then reducing the proton rate at the detector with a range of circular brass collimators between 1 mm and 30 mm in diameter. The best results were achieved with a 1.98 mm collimator.

The CAEN digitiser records the signal from the PMT and depending on the mode of operation, either integrates the signal and outputs the integrated charge, or outputs the raw waveform. This information is output via USB and recorded on the controlling PC.

Figure 16: *Setup of the light-tight box (black) containing the Hex calorimeter module, on the patient treatment chair (white). The nozzle of the proton beam can be seen to the right. The detector has not yet been raised to appropriate height.*

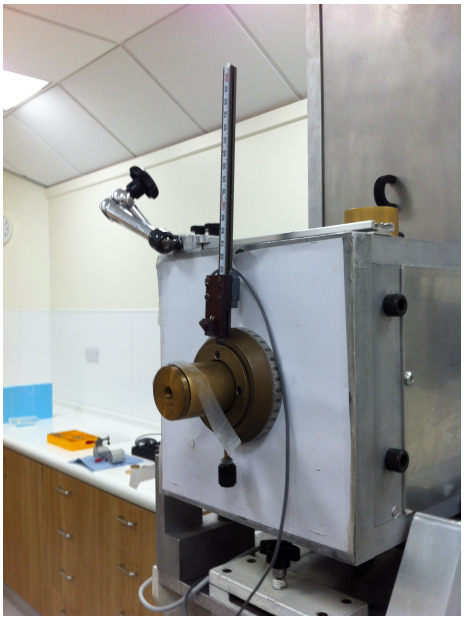

Figure 17: *Close-up of nozzle. Brass collimator can be seen inserted in position at the front, but without securing cuff.*

7.1 EJ-Block Module

The Hex module is not optimised for the high event rates required for pCT. As such, a smaller module based on the same construction but with a smaller scintillator block and PMT was developed to provide improved timing resolution. This module consists of a 3-inch Hamamatsu R6233-100SELECT PMT, coupled with RTV-615 optical gel to an ELJEN EJ-204 PVT [16] scintillator block of size $40 \times 40 \times 50\,\text{mm}$ and is referred to hereafter as the "EJ-Block". The EJ-204 PVT block has a scintillation efficiency of ∼10,400 photons/1 MeV e^- and a maximum wavelength emission of 408 nm, as seen in Fig. 19. The R6233 PMT bi-alkali photocathode, as shown in Fig. 12 (blue line), is from Hamamatsu's Super Bialkali range and has typical quantum efficiency of 35% at peak wavelength of 350 nm and 34% at 400 nm [12]. The block is wrapped in three layers of 75 μm thick PFTE tape and two layers of 6 μm (12 μm total) thick mylar glued together with RTV-615 so as to reflect escaping light back into the scintillator.

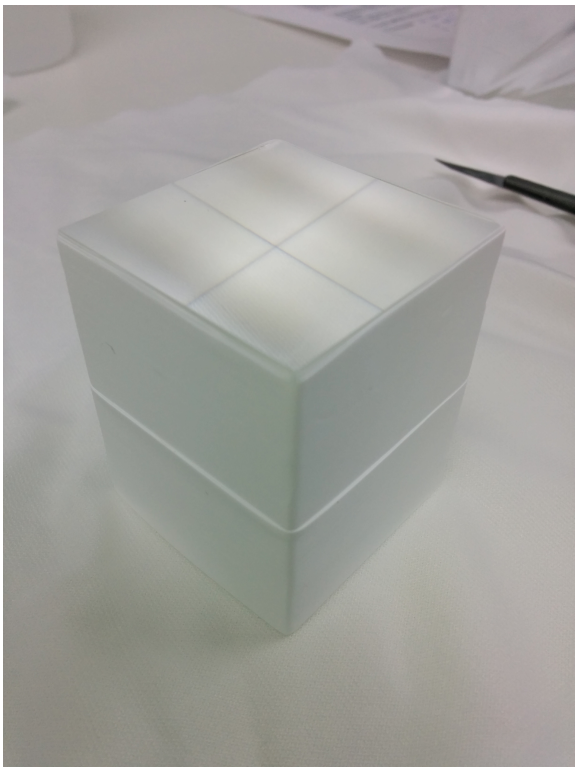

Figure 18: *The EJ-204 PVT scintillator block.*

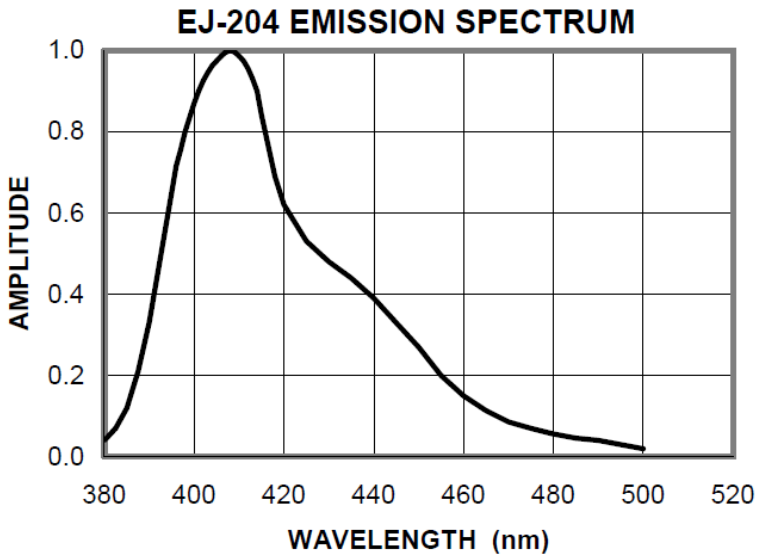

Figure 19: *Emission spectrum for ELJEN EJ-204 PVT plastic scintillator [16], used with the "EJ-Block" detector.*

7.1.1 EJ-Block Energy Resolution Analysis

To test the energy resolution performance of the smaller "EJ-Block" module, data in the form of ADC spectra were taken at Clatterbridge on the 9th July 2015 (day two of the July 2015 Clatterbridge run). The module was run with a PMT bias voltage of 700 V with the 60 MeV clinical proton beam during the tests. In order to obtain the curve for energy resolution as a function of energy, a range of energy points was needed. To obtain these, PMMA modulators of 0 mm (i.e. no modulator inserted), 5.07, 9.80, 14.12, 17.94, 19.94 and 21.71 mm — the same thicknesses used in prior test runs — were used to change the energy of the incoming beam. An example of the raw ADC spectra produced by the CAEN digitiser from the EJ-Block can be seen in Figure 20. An example of the raw output of the PMT for a single proton is shown in Figure 21.

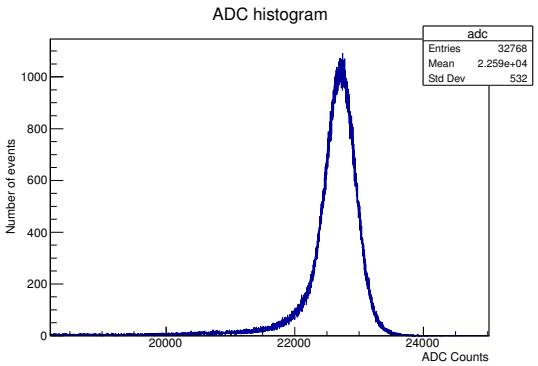

Figure 20: *Raw ADC spectrum for beam passing through 5.07 mm of PMMA, as recorded with the EJ-Block.*

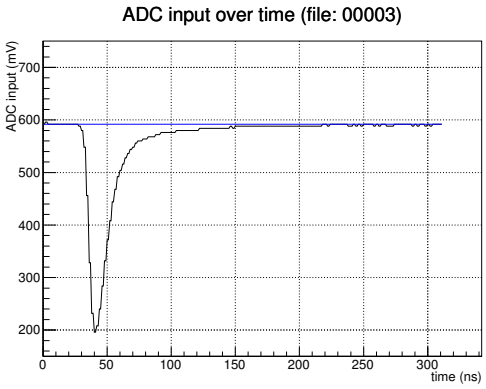

Figure 21: *Raw waveform data for beam passing through 5.07 mm of PMMA, as recorded with the Hex module. Baseline can be seen in blue.*

The statistical nature of ionisation energy loss leads to fluctuations in the amount of energy deposited by a particle traversing an absorber. For particles traversing a thin layer of material this results in the characteristic Landau distribution of energy deposition. The emerging beam therefore has a "mirrored" Landau energy spread.

To obtain an energy resolution from the data, (as per Equation 11) the distribution of each ADC spectrum for different PMMA thicknesses (beam energies) was fitted first with a Gaussian from which the value of σ was used to set a range of $[-4.5\sigma, +3\sigma]$ for the main fit. The main fit consists of a Landau-Gaussian convolution with a "mirrored" Landau tail that extends out towards the lower energies to the left of the peak as opposed to the usual higher energies on the right, with another non-reflected and non-broadened Landau on the right. Examples are shown in Figs. 22 and 23.

As access to the proton beam was limited, evaluation of the uncertainties could

not be completed by repeating the test measurements. Estimates of fitting uncertainties were obtained by repeating the Landau-Gaussian fit over varying ranges of σ (Table 1). The systematic error of the fit for a given PMMA point was taken as half the range between the worst and best resulting energy resolutions over all the different ranges of fits for that point. The energy resolution as a function of proton energy, with associated errors, can be seen in Fig. 24.

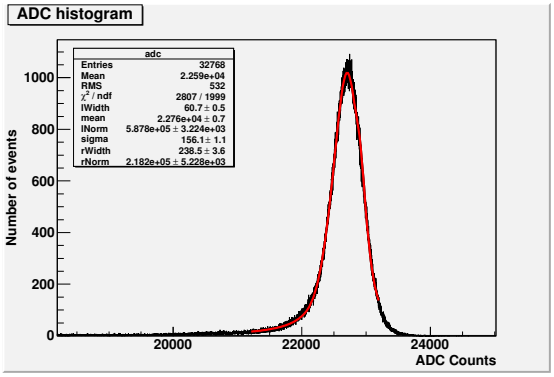

Figure 22: *Fit with lower limit of -5σ and upper limit of 1.5σ of the initial Gaussian fit for beam passing through 5.07 mm of PMMA.*

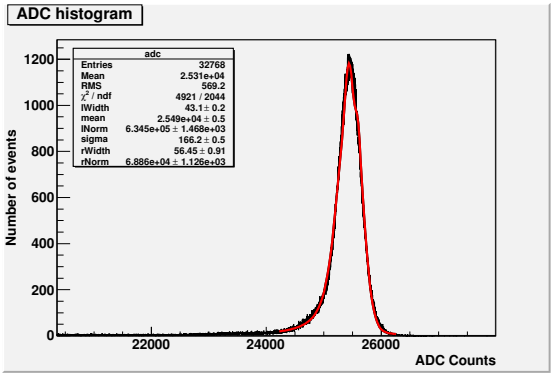

Figure 23: *Fit with lower limit of -4.5σ and upper limit of 3σ of the initial Gaussian fit for beam passing through 0 mm of PMMA (no modulator).*

The fit to the data is of the form:

$$\frac{p_0}{\sqrt{E}} + p_1 + \frac{p_2}{E} + p_3 E \tag{13}$$

with p_0 restricted to positive values and shows the expected improvement with increasing energy on the total energy resolution (Equation 9). The inclusion of the term $p_3 E$, which initially seemed to suggest a potentially unknown third component of electronic noise that increased proportionally with energy, was implemented based on what appeared to be an improved fit to the data after its inclusion. Though this empirical fit appears to conform well to the data, it is not possible to give with certainty a physical interpretation to the parameter values that are returned.

Errors are larger for lower values of proton E, as lower energies were achieved by passing the proton beam through thicker blocks of PMMA. The greater amount of material the beam has to traverse leads to increased energy straggling. This new setup gives an energy resolution of $1.533 \pm 0.225\%$ FWHM ($\sigma = 0.652\%$) for ADC data from 60 MeV protons, below the 1% uncertainty requirement for pCT.

Table 1: *Ranges of σ (obtained from an initial Gaussian fit) over which the modified Landau-Gaussian convolution fit is varied for the ADC spectra obtained from passing through PMMA blockers of varying thickness. The -4.5σ, $+3\sigma$ range used for the main fit to obtain an energy resolution is shown in bold.*

Range in σ		Energy resolution (% FWHM) for varying PMMA thickness						
Lower limit	Upper limit	0 mm	5.07 mm	9.8 mm	14.12 mm	17.94 mm	19.94 mm	21.71 mm
-1.5	1.5	1.108 ± 0.013	1.501 ± 0.019	2.935 ± 0.018	2.883 ± 0.017	4.327 ± 0.022	4.795 ± 0.085	7.154 ± 0.081
-2.5	2.5	1.461 ± 0.007	2.043 ± 0.009	3.070 ± 0.012	3.626 ± 0.009	5.187 ± 0.011	6.793 ± 0.023	7.315 ± 0.062
-3.5	1.5	1.145 ± 0.011	1.585 ± 0.012	2.328 ± 0.019	3.493 ± 0.016	5.063 ± 0.018	6.615 ± 0.026	9.228 ± 0.039
-4	2.5	1.399 ± 0.005	2.034 ± 0.007	3.069 ± 0.010	3.623 ± 0.007	5.173 ± 0.011	6.764 ± 0.017	9.228 ± 0.039
-4.5	**3**	$\mathbf{1.533 \pm 0.005}$	$\mathbf{2.095 \pm 0.006}$	$\mathbf{2.614 \pm 0.010}$	$\mathbf{3.630 \pm 0.007}$	$\mathbf{5.185 \pm 0.011}$	$\mathbf{6.762 \pm 0.017}$	$\mathbf{9.228 \pm 0.039}$
-4.5	3.5	1.540 ± 0.005	2.116 ± 0.005	3.157 ± 0.007	3.630 ± 0.007	5.185 ± 0.011	6.762 ± 0.017	9.228 ± 0.039
-5	3	1.558 ± 0.004	2.099 ± 0.006	3.151 ± 0.007	3.636 ± 0.007	5.193 ± 0.009	6.764 ± 0.015	9.228 ± 0.039
-5	2.5	1.486 ± 0.006	2.049 ± 0.007	3.081 ± 0.008	3.632 ± 0.007	5.193 ± 0.009	6.763 ± 0.017	9.228 ± 0.039
-5	2	1.419 ± 0.008	1.994 ± 0.019	2.989 ± 0.012	3.579 ± 0.010	5.188 ± 0.011	6.735 ± 0.021	9.228 ± 0.039
Final:		1.533 ± 0.225	2.095 ± 0.307	2.614 ± 0.414	3.630 ± 0.377	5.185 ± 0.433	6.762 ± 0.999	9.228 ± 1.037

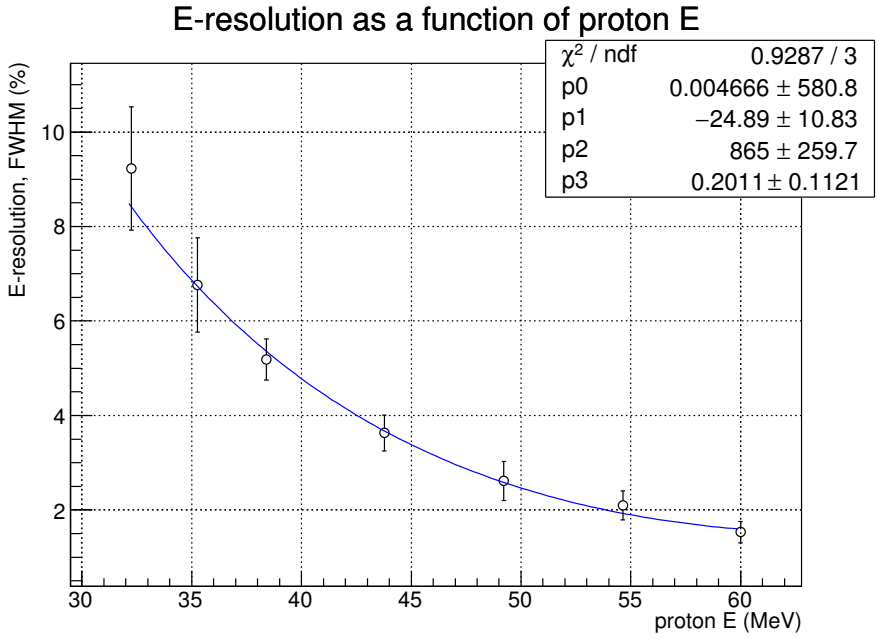

Figure 24: *Plot of energy resolution (% FWHM) obtained from the fitted σ of the ADC spectra of the EJ-Block as a function of proton energy (MeV).*

7.2 Waveform Discrimination via Pulse-Shape Analysis

While the current energy resolution for the Hex detector has been on the order of $\sigma \sim 0.67\%$. ($\sim 1.57\%$ FWHM), which is within the levels deemed necessary for pCT, this has so far only been achieved with low rates of protons. An increase in rate typically leads to worse energy resolution, likely owing to increased levels of pulse pile-up — when pulses arrive closer in time than the resolution time for the system, potentially overlapping a previous pulse before it has returned to baseline levels (Figure 25). As pulse pile-up events can occur anywhere on a waveform (see Figure 26), there is limited effectiveness in narrowing of the integration gate time.

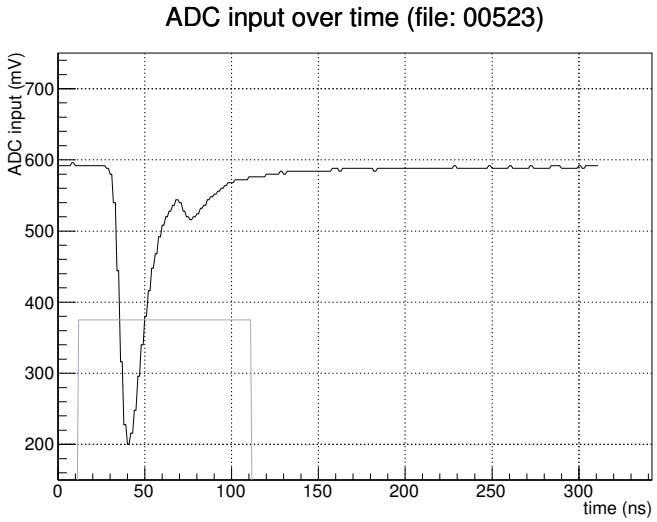

Figure 25: *Example of pulse-pile up within the duration of the recorded waveform. A smaller pulse, which may be a proton that potentially escaped the scintillator before depositing all of its energy, or some other secondary particle generated along the beamline such as when the proton beam hit the collimator, can be seen overlapping the first pulse inside of the integration gate at* $\sim 80\,ns$.

An attempt was made to construct an algorithm for pulse-shape analysis from which to determine incidents of pulse pile-up in the recorded data and the systematic rejection of such events so as to clean up the spectra and improve energy resolution. The CAEN digitiser is capable of digitising and recording the waveform of every single pulse in a single continuous .dat file. Two sample waveform files were recorded with the Hex module: the first at lower rates of $\sim$ 500 Hz–2 kHz to obtain some data with reduced chances of pileup and the second at higher rates of $\sim 200\,\text{kHz}$–$300\,\text{kHz}$. The record length of each waveform was set to 312 ns after visually inspecting the shape of individual waveforms from the CAEN digitiser in real-time so as to record the entire pulses whilst giving enough time for the waveform to return to the baseline value. The long gate for both datasets was set to 100 ns.

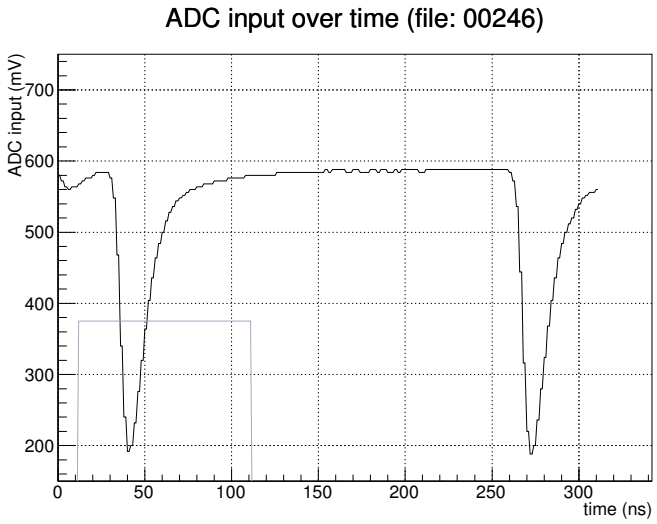

Figure 26: *Example of pulse-pile up within the duration of the recorded waveform. A small pulse not large enough to trigger recording of the waveform can be seen at* ~ 5 *before the large pulse at* $\sim 40\,ns$*, both within the integration gate. Another large pulse can be seen at* $\sim 270\,ns$ *outside of the integration gate.*

The fit to each waveform, $f(t)$, is a piecewise function approximated as two straight lines and an exponential, which map to the pedestal, rising edge of the pulse and the fall-off/decay of the pulse respectively (Equation 15). As the baseline, the pedestal should be a near constant value and the rise of the pulses were steep enough that both were approximated as straight lines for the sake of simplicity. The decay of the signal should be exponential in nature on account of the exponential de-excitation of the scintillator fluor molecules. This was kept as a single exponential for simplicity. The fitting of function $f(t)$ was calculated via the least-squares method using ROOT's own fitting function (TH1::Fit) with the errors all set to 1, which performs the χ^2 least-square fit (Equation 14), where $y(i)$ is the observed value for each point i, $x(i)$ is the expected value and $e(i)$ is the error.

$$\chi^2 = \sum \frac{(y(i) - x(i))^2}{e(i)} \tag{14}$$

Parameters p_0 through to p_8 are parameters of the fit and require initial values as start points. The code initially fits each section of the waveform in turn (see Fig. 27a), then refits the final overall waveform with parameters 2–6 free. For the initial fits to the separate sub-ranges of the graph, p_0 and p_1 are free parameters for the first part of equation 15, fitted from $t = 0$ to the point at which the pulse begins to rise. p_0 and p_1 are seeded with approximate starting values obtained from an average of the first 10 ADC input values of each waveform. The second part is fitted from the point the pulse begins to rise through to the point at which the minimum

ADC input value of the graph occurs; p_2 and p_3 are free parameters and p_0 and p_1 are bound as the values obtained from the fit to the previous section. The third part is fitted from the peak through to the end of the waveform, with p_0 through to p_3 held fixed (values obtained from fit to previous section) and p_4 to p_8 as free parameters. p_7 and p_8 are additional linear components to account for the offset of the exponential section not falling back to the original baseline.

$$f(t) = \begin{cases} p_0 + p_1 t & \text{for } (t < p_2) \\ p_0 + p_1 t + p_3(t - p_2) & \text{for } (p_2 < t < p_4) \\ p_0 + p_1 t + p_7 + p_8 t + p_3(p_4 - p_2) p_6 e^{-p_5(t-p_2)} & \text{for } (t > p_4) \end{cases} \tag{15}$$

where: p_0 = pedestal, (mV)
p_1 = pedestal walk, (mVs^{-1})
p_2 = signal growth/rise point, t (ns)
p_3 = gradient of growing pulse, (mVs^{-1})
p_4 = point pulse stops growing/peak, t (ns)
p_5 = decay constant for the exponential term, (s^{-1})
p_6 = normalisation factor for the exponential term
p_7 = baseline shift, (mV)
p_8 = gradient of shifted baseline, (mVs^{-1})

The overall total fit (Fig. 27b) to the waveforms returns a χ^2 value and NDF (number of degrees of freedom), where reduced χ^2 (χ^2_{red}) is χ^2/NDF. The resulting χ^2_{red} values obtained from the fits to every waveform in a dataset were passed to a histogram in order to see the χ^2_{red} distributions. Based on where there was a sharp drop-off in values in the χ^2_{red} distributions, (see Fig. 28a and Fig. 28b respectively) an acceptance limit for χ^2_{red} of $\sim$100 was chosen for both the lower and higher rate waveform data. For waveforms that were found to be within acceptable χ^2_{red} limits, the waveform was integrated for the same duration as the automatic ADC spectrum generated to obtain the integrated charge. This value was then passed to a separate histogram in order to obtain an energy spectrum without the contribution from waveforms that were identified and filtered out as potentially contaminated with pulse pile-up.

The fraction of waveforms retained (number of waveforms passing the cut/number of waveforms) was found to be 99.7% for reduced χ^2 (χ^2_{red}) window of 0–100 when applied to the lower rate data set. Purity (number of good waveforms/number of waveforms passing the cut) for the lower rate waveforms found to be within the window were assessed by eye-scanning the first 100 waveforms, of which none displayed multiple peaks within the recorded length. Peaks approximately $> 10\,\mathrm{mV}$ could be discerned visually as separate pulses (see Figure 29). An example of a small pile-up event can be seen in Fig. 30a. False-positive identification of "bad" waveforms (those

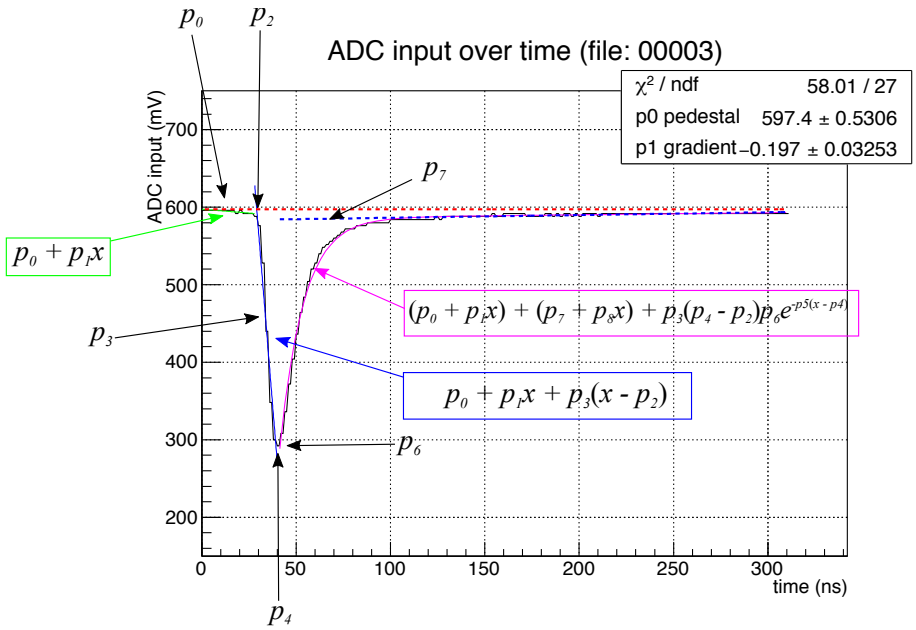

(a) *Separate fits to different ranges of ADC input waveform to obtain starting values for total fit.*

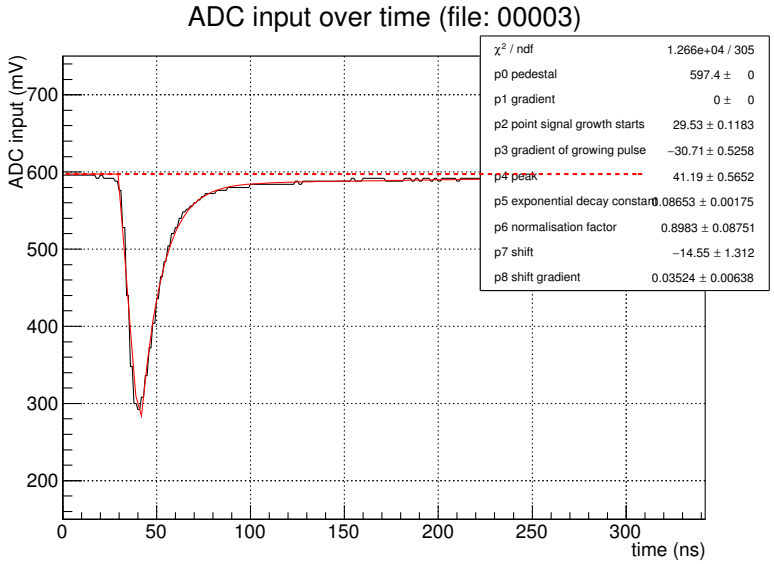

(b) *Total fit (red line) to an ADC input waveform.*

Figure 27

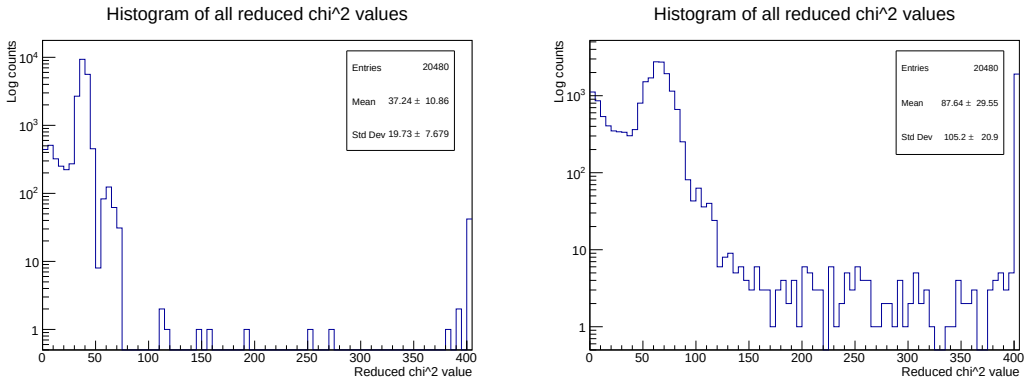

(a) **(b)**

Figure 28: *Reduced χ^2 distributions of the fit to* ***(a)*** *lower rate data; $\sim 500\,Hz$–$2\,kHz$ and* ***(b)*** *higher rate data; ~ 200–$300\,kHz$, where the final bin includes the overflow.*

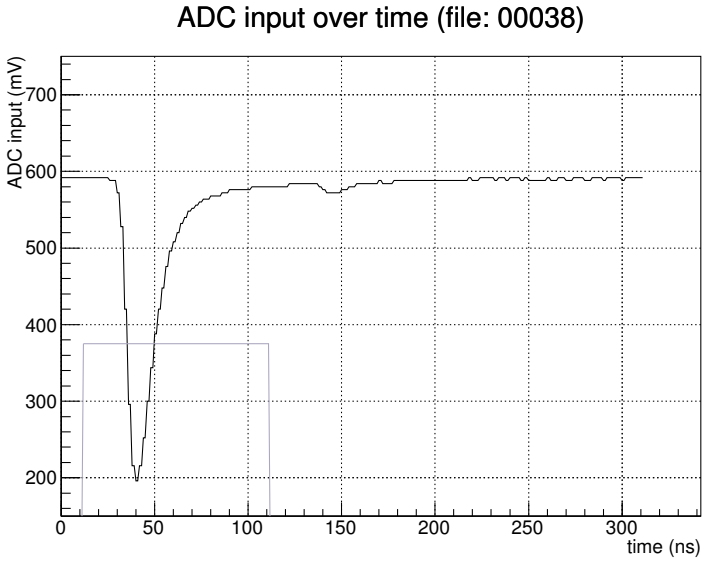

Figure 29: *A waveform from the higher rate ~ 200–$300\,Hz$ dataset. A smaller separate pulse of $\sim 10\,mV$ can be seen to the right of the main pulse at $\sim 150\,ns$.*

that returned a poor χ^2_{red} value but were free of pile-up when investigated by eye-scanning) found 50 out of the 53 total waveforms (94.3%) identified in the lower rate dataset were in fact free of pile-up. For the higher rate data set, the fraction retained was found to be 89.0% and a purity of 99% for the first 100 eye-scanned waveforms. False-positive fraction naturally falls to 30% for the higher rate set, where occurrences of pulse pile-up events is higher. This could be a direct result of the higher frequency of the dataset with simply higher chance of more than one pulse being encountered more in the length of a waveform (in this case 311 ns) if one assumes that the protons arrive at a steady rate.

To check that the build-up of waveforms with low χ^2_{red} before the peak structure in the χ^2_{red} distribution histograms were not cases of the digitiser recording flat waveforms and the fit returning a low χ^2_{red} value as a result of fitting a straight line, the fraction retained, purity and fraction of false positives were checked for $10 < \chi^2_{\text{red}} < 100$ and $20 < \chi^2_{\text{red}} < 100$. Purity and fraction of false positives were checked by outputting the first 100 bad waveforms to a discrete folder for offline analysis. While the fraction retained for both the low and high rate sets has decreased, purity remains the same, with the false-positive fraction increasing.

Table 2: *Summary of fraction retained, purity and false positive pile-up identification percentiles of the fits using two straight lines and an exponential to waveform data for different event rates taken during the July 2015 run at Clatterbridge.*

Run	Rate kHz	χ^2_{red} window	Number of waveforms Total	Accepted	Fraction retained %	Purity %	False positive %
079	0.5–2	0–100	20480	20427	99.7	100	94.3
		10–100		19476	95.1	100	99.0
		20–100		18903	92.3	100	99.0
093	200–300	0–100	20480	18234	89.0	99	30.0
		10–100		16258	79.4	99	60.0
		20–100		15316	74.8	99	67.0

Eye-scanning the first 100 waveforms outside the χ^2_{red} limits for both low and high-rate datasets found increased numbers of false-positive identifications from waveforms of reduced $10 < \chi^2_{\text{red}}$ and $20 < \chi^2_{\text{red}}$ obtained from fits to small waveforms (see Fig. 30b), with none found to be from flat straight-line fitted waveforms. This suggests that waveforms outside the peak in the distribution which appears to start at $20 < \chi^2_{\text{red}}$ do not contain or contained very few flat waveforms (as recording would not have been triggered anyway) or that fits to smaller waveforms which have a much less steep rise and fall to the pulse return better χ^2.

Efficiency and percentile of false-positives will have some effect from the simplified fit function and may potentially improve with the fitting of a more complex function in the future. Fitting with a more complex function which can conform more closely with the expected shape of the pulses should lead to lower χ^2_{red} values and make

the fit more sensitive to deviations to that shape. This will lead to potentially more obvious distinctions between structures such as the peaks containing pure waveforms and contaminated waveforms in the χ^2_{red} distribution histograms.

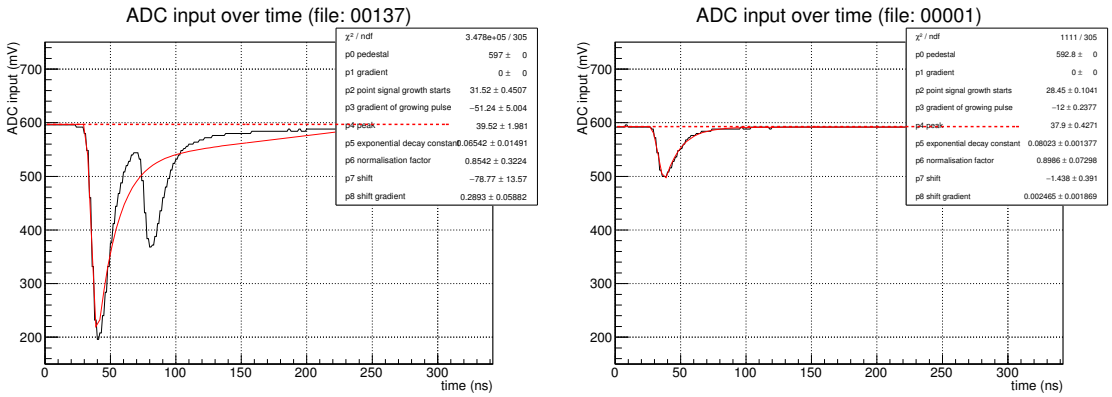

(a) *A pulse pile-up event with two proton peaks.* **(b)** *Small waveform with no visible pile-up.*

Figure 30: *First "bad" waveform filtered out from the higher rate data set with* ***(a)*** $0 \leq \chi^2_{red} < 100$ *filter and* ***(b)*** $10 \leq \chi^2_{red} < 100$ *filter applied.*

Comparison between the unfiltered and $0 \leq \chi^2_{\text{red}} < 100$ filtered pulse-integrated ADC spectra can be seen for the lower and higher rate data set in Figs. 31a and 31b respectively. Most pulses at integrated ADC values greater than ~ 11000 beyond the peak of the pulse-integrated histogram have been filtered out. A noticeable number of pulses before the falling edge of the peak at $\sim 10,000$ have also been filtered out. For the lower rate dataset, energy resolution from fitting the resulting reconstructed ADC spectrum via the same method and ranges as given in Sec. 7.1.1 was found to be $2.933 \pm 0.183\%$ FWHM without a filter applied and $2.932 \pm 0.182\%$ with a $0 \leq \chi^2_{\text{red}} < 100$ filter (Fig. 32a). Though there is no significant improvement, the fraction retained after filtering was 99.7% and unlikely to have made a significant difference to the spectrum. There is no clearly defined peak for the higher rate data and no satisfactory fit (Fig. 32b). For the fit to the ADC spectrum recorded directly from the digitiser for the same lower rates of $\sim 500\,\text{Hz}$–$2\,\text{kHz}$ on the same day, an energy resolution of $2.366 \pm 0.012\%$ was found (Fig. 33).

Comparison of the peak ADC input value distributions (Fig. 34) for both datasets show the data for the higher rate dataset is split into a distinct peak at $\sim 400\,\text{mV}$ and a larger, slightly broader peak at $\sim 430\,\text{mV}$, whereas the peak distributions for the lower rate dataset peak at $\sim 315\,\text{mV}$. It was mentioned by the Clatterbridge operators that the running of the Clatterbridge accelerator at a higher duty factor than is normally used for clinical treatment may result in overheating of the ion and RF sources leading to fluctuations in the beam intensity. To check this, the datasets were investigated with respect to time by binning in subsets of 1000 pulses (Fig. 35).

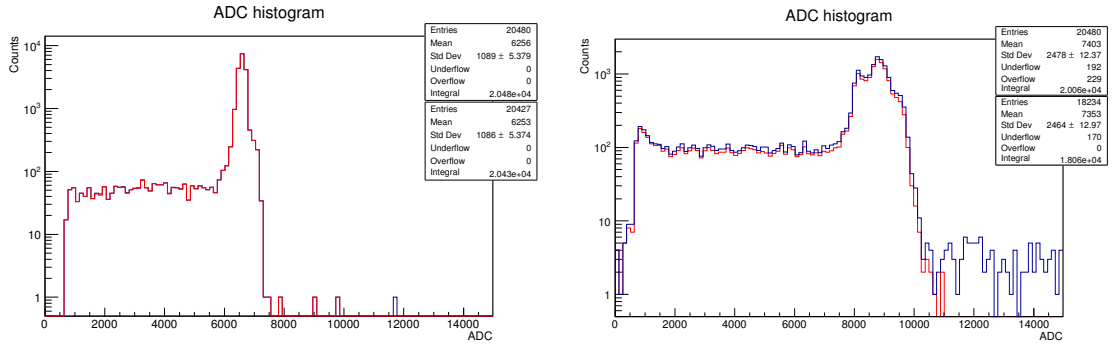

(a) $\sim 500\,Hz$–$2\,kHz$. **(b)** ~ 200–$300\,kHz$.

Figure 31: *Pulse-integrated values from waveforms in* ***(a)*** *lower rate dataset and* ***(b)*** *higher rate* ~ 200–$300\,kHz$ *dataset, before filtering (blue) and after* $0 \leq \chi^2_{red} < 100$ *filter is applied.*

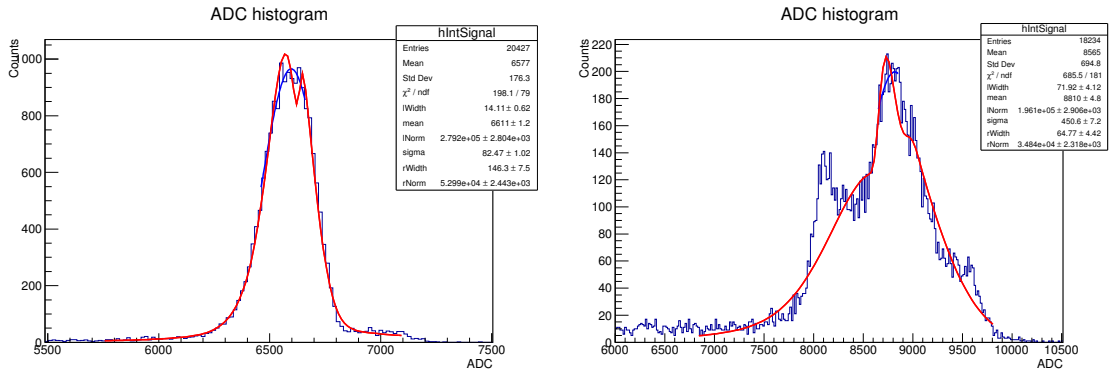

(a) $\sim 500\,Hz$–$2\,kHz$. **(b)** ~ 200–$300\,kHz$.

Figure 32: *Landau-Gaussian convolution fit over a* -4.5σ *to* 3σ *range to the* ***(a)*** *lower rate and* ***(b)*** *higher rate pulse-integrated histogram post-filtering with* $0 \leq \chi^2_{red} < 100$ *cut.*

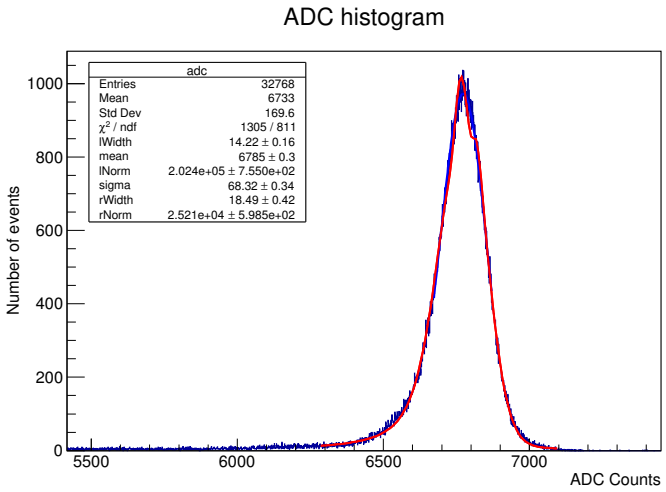

Figure 33: *Landau-Gaussian convolution fit over a -4.5σ to 3σ range to the ADC spectrum obtained directly from the digitiser for a $\sim 500\,Hz$–$2\,kHz$ rate dataset obtained on the same day.*

Comparison of the ADC spectra for the waveform subsets (plotted in a TH2D histogram) for the lower rate data set shows that the mean ADC value is relatively stable with a peak in intensity (Fig. 35a). Comparison for the higher rate dataset shows the mean energy shifting over the 1000 pulse subsets — and therefore in time — often with no clear peak in the subsets (Fig. 35b), potentially as a result of the aforementioned beam instability after long run times. This is potentially a result of the frequency-dependant nature of the PMT gain with a change in intensity then leading to a perceived shift in the reconstructed energy spectrum.

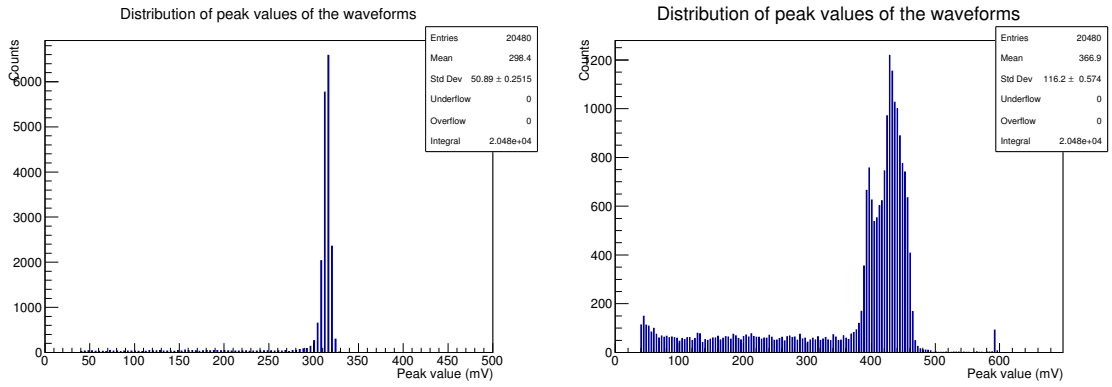

(a) **(b)**

Figure 34: *Distribution of peak ADC input values of the pulses for **(a)** lower rate and **(b)** higher rate datasets.*

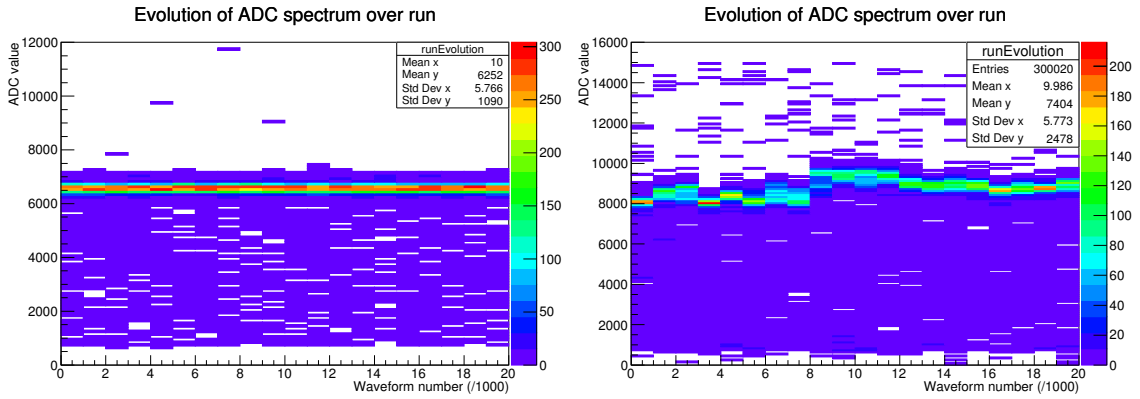

(a) **(b)**

Figure 35: *Evolution of ADC values per 1000 pulses for* ***(a)*** *the* $\sim 500\,Hz$–$2\,kHz$ *lower rate dataset and,* ***(b)*** *the* 200–300 *kHz dataset.*

An attempt was made to extract an energy resolution from the higher rate data set by fitting the mirrored Landau-Gaussian function (to account for the mylar foils) used in Section 7.1.1 to a subset consisting of the first 1000 pulses post-filtering with a $0 \leq \chi^2_{\text{red}} < 100$ cut, where there appears to be a clearer peak in the data (Fig. 36). Although the fit to the subset shows an improved energy resolution of $2.279 \pm 0.194\%$ FWHM, statistics for the subset are low, with only 893 waveforms remaining after filtering with a $0 \leq \chi^2_{\text{red}} < 100$ cut.

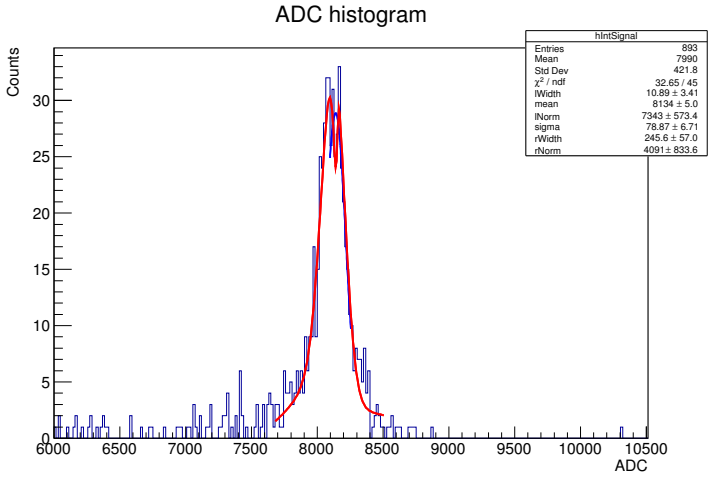

Figure 36: *Landau-Gaussian convolution fit over a* -4.5σ *to* 3σ *range to the first 1000-pulse subset of the higher rate dataset, post-filtering with* $0 \leq \chi^2_{red} < 100$ *cut.*

While the filter appears to working correctly in the exclusion of a large proportion of waveforms containing more than one pulse, albeit with potential for improvement

in the false-positive identification of bad waveforms, it does not appear to be the case that pulse pileup is responsible for significant broadening of the ADC spectrum. During the course of constructing the fit for these data, it was found that the value of the baseline for the baseline-subtraction prior to pulse integration significantly affected the charge-integrated ADC spectrum. This is investigated in the next section.

7.3 Baseline Subtraction

The ADC spectra from which the energy resolutions are obtained are highly sensitive to the choice of baseline used for baseline-subtraction prior to pulse integration (Fig. 37). Baseline subtraction with use of the CAEN-recorded baseline results in an ADC spectrum that has a small shoulder at energies slightly higher than that of the main peak, which is at ~ 6600 ADC (see Fig. 37a). Baseline subtraction using the maximum ADC input value found for each waveform results in a double-peaked energy spectrum (Fig. 37b). For baseline subtraction where the baseline is taken as the constant term p_0 from the overall fit of Eq. 15 to each waveform, the ADC spectrum where the initial fit to the first section has a free gradient p_1 (Fig. 37c) displays a smaller peak at energies slightly higher than that of the main peak (~ 6700) at ~ 7000. This can be seen in Fig. 37b where the maximum ADC input value is taken as the baseline, as an even greater peak at ~ 6950. Where the baseline was obtained from the initial fit to the first section as a single parameter with no gradient (Fig. 37d), this higher peak has merged with the higher-energy side of the ~ 6600 peak, shifting the overall mean energy to ~ 6700.

As the ADC input values are quantised to multiples of 4, so too are the CAEN-recorded baseline values. Over the long gate of 100 ns this means a change in the baseline value of a single quanta can result in a ~ 400 ADC change in the integrated ADC value, giving an error of $\sim 6\%$ for a mean integrated ADC charge of 6611 mV for the lower rate dataset.

While the contribution of the baseline may not alone be sufficient to explain broadening of the high-rate spectra, it is clearly a large effect. Though further investigation is needed in this area, the value used for the purposes of baseline subtraction will henceforth be taken as a single parameter (i.e. no gradient) from the initial fit to the flat portion of the waveform as the shape of the integrated waveform histogram this returns is the most similar out of the investigated options to the ADC spectra usually seen and recorded by the digitiser.

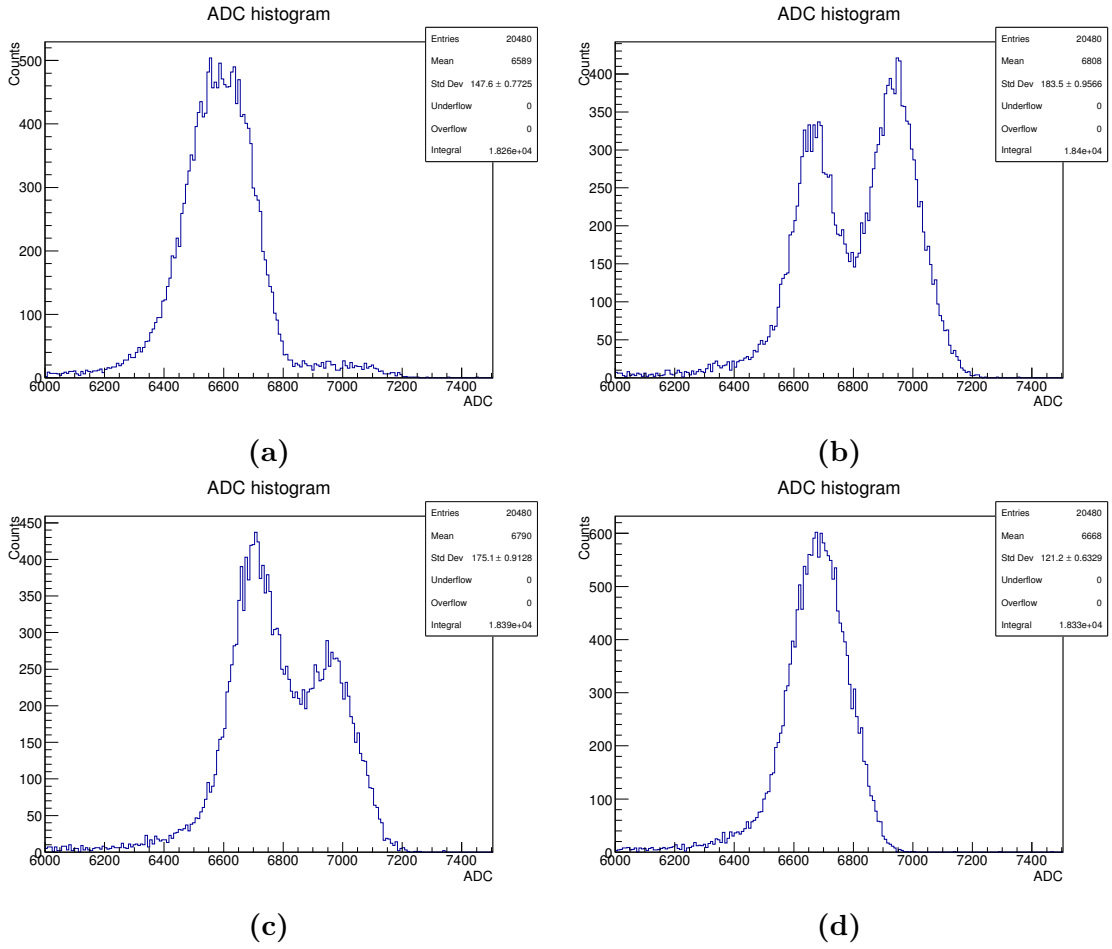

Figure 37: *ADC spectra for the same lower rate* $\sim 500\,Hz$*–*$2\,kHz$ *data file with baseline choice for baseline-subtraction prior to pulse-integration taken from* ***(a)*** *digitiser data-file recorded,* ***(b)*** *maximum ADC input value for each waveform,* ***(c)*** *baseline as given by the constant term of the fit, where the initial fit to the flat portion of the waveform has a gradient and* ***(d)*** *baseline as given by the fit, where the initial fit to the flat portion of the waveform is held fixed as having no gradient.*

8 Enhanced Cuboid Module Tests

In order to further improve the timing resolution of the system, a new, smaller module (referred to hereafter as the enhanced cuboid module) was designed, with the smaller scintillator block intended to enable faster and greater light collection. Tests with this cuboid module were carried out at Clatterbridge on 21st and 22nd December 2015.

8.1 Enhanced Cuboid Module

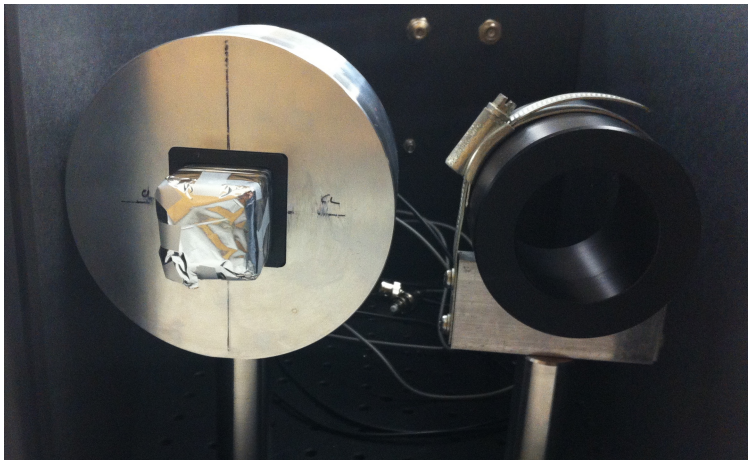

Figure 38: *Cuboid module set in holder inside the light tight box.*

The cuboid module detector consisted of a 2-inch Hamamatsu R13089-100-11 PMT coupled using BC-630 Saint Gobain silicone optical gel of refractive index 1.465 with a 3 × 3 × 5 cm cuboid NUVIA enhanced PS scintillator (Fig. 38). This is smaller than the 27.6 cm diameter and 19.3 cm deep hexagonal block of PVT used to construct the Hex module and reduces the time it takes for scintillation light to reach the PMT. The R13089 PMT photocathode is from Hamamatsu's current bialkali range and has a spectral response from 300 to 650 nm with quantum efficiency of $\sim 25\%$ at peak wavelength of 450 nm as shown in Fig. 12 (grey line) [12]. As with the previous detector, the NUVIA scintillator is wrapped in three layers of PTFE tape and two layers of 6 μm-thick aluminised mylar (12 μm total) coupled together with the BC630 gel.

8.2 Waveform Discrimination via Pulse-Shape Analysis

Comparison of the integrated waveform ADC values (Fig. 39) for one of the 25 kHz datasets showed a split into a distinct peak at $\sim 9,500$ mV and a larger peak at $\sim 11,000$ mV. Investigating with respect to time by binning in subsets of 1000 pulses (Fig. 40) shows a sharp jump in the mean of the integrated waveform histograms at $\sim 61,000$ waveforms.

Investigating the first 100 waveforms by eye revealed that the majority of the pulses (which are negative waveform pulses) extended from the baseline all the way down to 0 mV, where they were clipped (see Fig. 41), potentially indicating saturation of the PMT. While several waveform files were obtained, subsequent analysis of the waveforms found that the majority were clipped at 0 mV, making it impossible to obtain an accurate charge-integrated ADC value for the pulses in question. An attempt was made to obtain an energy resolution from the dataset by fitting to a peak obtained from integrating only waveform numbers $< 60,000$ (before the jump in mean ADC value) in addition to removal of all waveforms with ADC hitting 0 mV, however as the percentage of waveforms retained was 5.91% (56454/60000), leaving only 3546 entries, a fit could not be obtained from the resulting integrated waveform histogram histogram (Fig. 42).

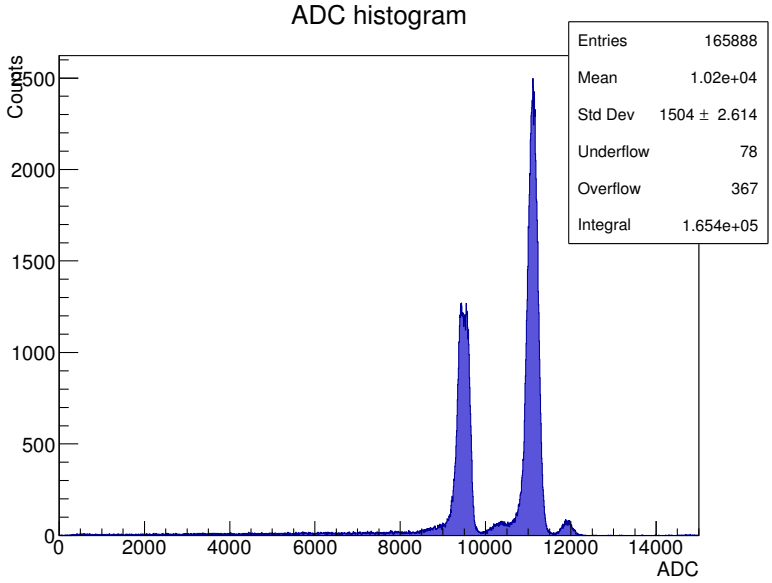

Figure 39: *Evolution of ADC values per 1000 pulses for the* ~ 25 *kHz waveform dataset obtained during the December 2015 run at Clatterbridge.*

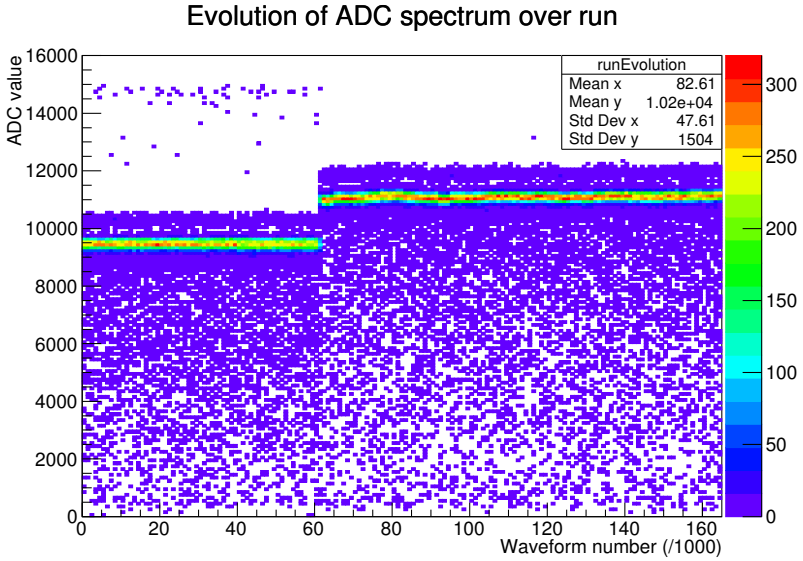

Figure 40: *Evolution of ADC values per 1000 pulses for the* $\sim 25\,kHz$ *waveform dataset obtained during the December 2015 run at Clatterbridge.*

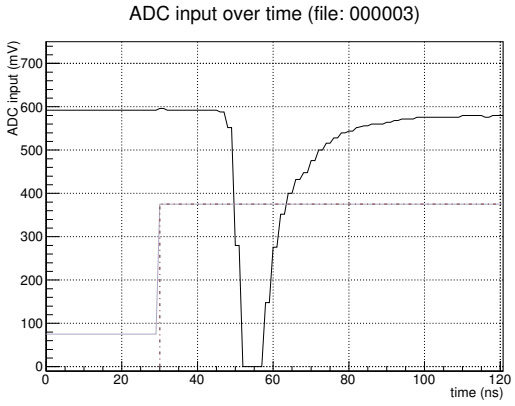

Figure 41: *Example of a waveform pulse clipping at* $0\,mV$ *ADC.*

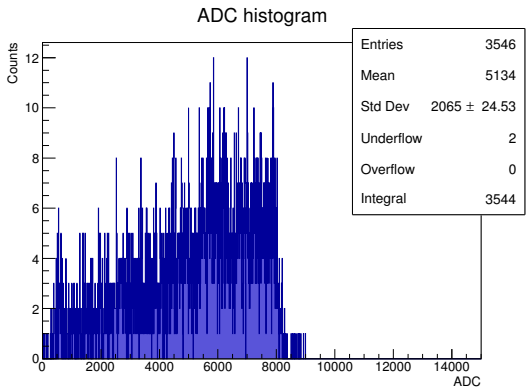

Figure 42: *Pulse-integrated ADC histogram of the first* $60,000$ *events from a* $25\,kHz$ *dataset, with all pulses which reach* $0\,mV$ *ADC filtered out, obtained with the enchanced cuboid module.*

9 Improved Waveform Discrimination

The second test beam run to obtain waveform data for the enhanced cuboid module at took place on the 2nd and 3rd August 2016. This was accompanied by a new fitting algorithm using functions which match the shape of pulses more accurately in an attempt to improve the purity and false-positive identification rates when filtering out pulse pile-up in the waveform data.

9.1 Waveform Discrimination via Pulse-Shape Analysis: Gaussian and Exponential Fit

The newer fit to each waveform (Equation (16)), $f(t)$, is a piecewise function approximated as a straight line, a Gaussian and a biphasic exponential, which map to the pedestal, rising edge of the pulse and the fall-off/decay of the pulse respectively (Fig. 43a). Parameters p_0 through to p_9 are parameters of the fit and require initial values as start points. The code initially fits each section of the waveform in turn (see Fig. 27a), then refits the final overall waveform with parameters 2–9 free.

For the initial fits to the separate sub-ranges, p_0 is a free parameter for the first part of equation, fitted from 0 ns to the point the Gaussian fit starts (p_8). p_0 is seeded with an approximate starting value obtained from an average of the first 10 ADC input values of each waveform. The second part is fitted from where the Gaussian fit starts (some value of t from before the pulse starts to rise, found by manually checking the first few waveforms) through to ~ 10 ns past the minimum found ADC input value (x-axis) of the graph; p_1 to p_3 are free parameters while p_0 is bound as the value obtained from the previous fit to the pedestal section. The third part is fitted from the peak through to the end of the waveform, with p_0 held fixed (values obtained from fit to previous section) and p_4 to p_7 as free parameters. p_8 and p_9 are additional linear components to account for the offset of the exponential section not falling back to the original baseline. These parameters are all indicated on the waveform displayed in Figure 43a.

$$f(t) = \begin{cases} p_0 & \text{for } (t < p_8) \\ p_0 - p_1 \exp(-\frac{(t-p_2)^2}{2p_3^2}) & \text{for } (p_8 < t < p_9) \\ p_0 - (p_4 \exp(-p_5 t) + p_6 \exp(-p_7 t)) & \text{for } (t > p_9) \end{cases} \tag{16}$$

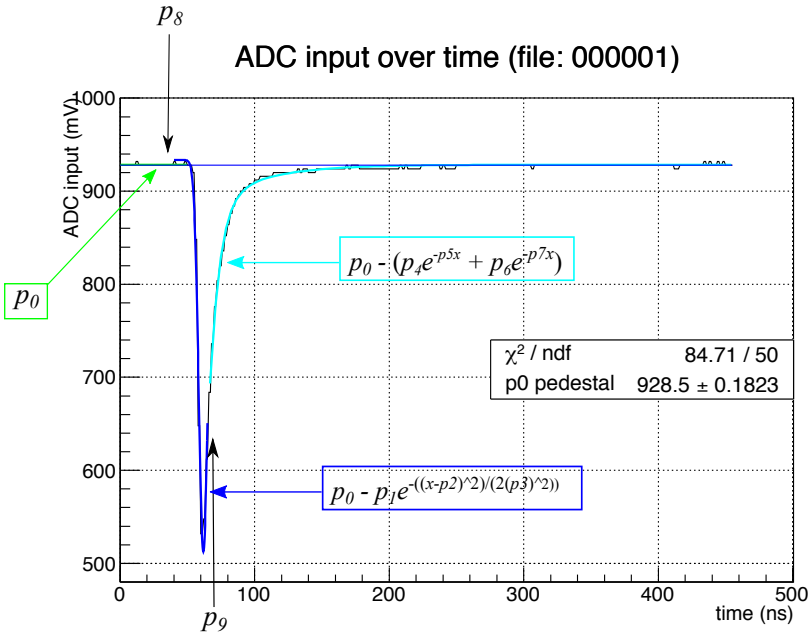

(a) *Separate fits of a straight line (green), a Gaussian (blue) and a biphasic exponential (aqua) to different ranges of ADC input waveform to obtain starting values for the total fit.*

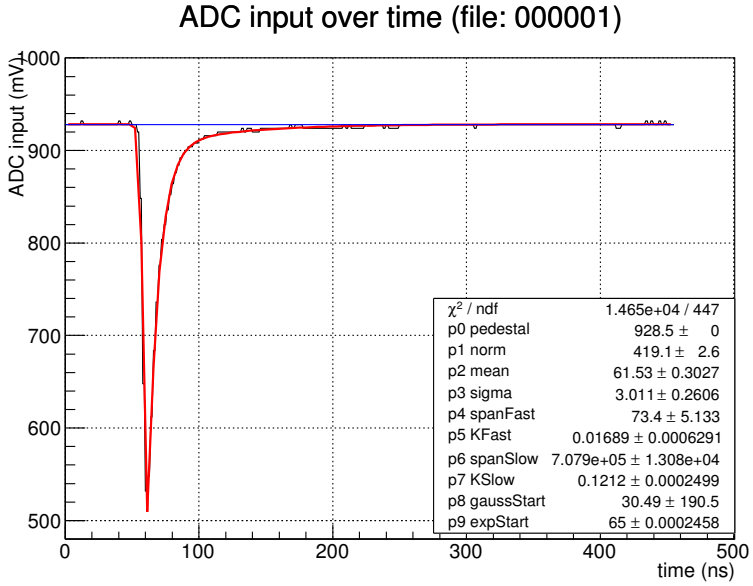

(b) *Total fit (red line) to an ADC input waveform.*

Figure 43

where: p_0 = pedestal, (mV)
p_1 = normalisation factor of the Gaussian
p_2 = mean of the Gaussian
p_3 = sigma of the Gaussian
p_4 = normalisation factor for fast exponential term
p_5 = decay constant for the fast exponential term
p_6 = normalisation factor for the slow exponential term
p_7 = decay constant for the fast exponential term
p_8 = point at which Gaussian starts, (t)
p_9 = point at which biphasic exponential starts, (t)

While this newer piecewise fit displays an improved fit to the waveform when inspecting by eye — particularly along the rising edge of the pulse — a discontinuity can be seen when under closer inspection where the Gaussian joins with the biphasic exponential potentially due to the asymmetrical shape of the waveform even at the tip. This can be seen at ~ 65 ns in Figure 44. Efforts to remove this discontinuity via the introduction of conditions upon acceptable values for the end of the Gaussian and start of the biphasic exponential could not be implemented successfully within the code. While this does not negate the use of the function as a fit for use in filtering based on returned χ^2_{red} values, a convolution of a Gaussian and biphasic exponential in the future should serve to remove this discontinuity.

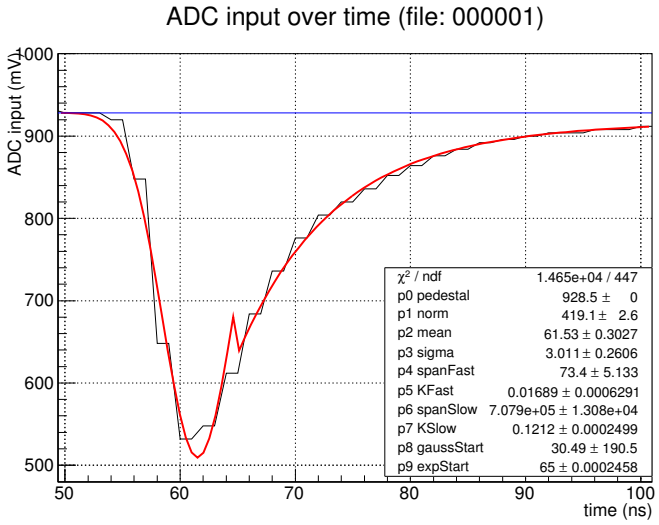

Figure 44: *Close-up of the rising and falling portion of the waveform with the piecewise Gaussian and biphasic exponential fit applied. A discontinuity can be seen to occur a* ~ 65 *ns, where the Gaussian ends and the biphasic exponential begins.*

Using this newer fit on the same 200–300 kHz higher rate dataset from the July 2015 run analysed earlier (see Table 2), the fraction of waveforms retained (number

of waveforms passing the cut/number of waveforms) was found to be 87.9% in comparison to the 89% obtained previously for reduced χ^2 (χ^2_{red}) window of 0–70. Purity for the lower rate waveforms found to be within the window were again assessed by eye-scanning the first 100 waveforms. While both the fraction retained and the purity remained similar to before, the false-positive identification of "bad" waveforms improved from 30% to 1%.

Table 3: *Comparison of fraction retained, purity and false positive pile-up identification percentiles of the fits using a Gaussian and biphasic exponential to waveform data for different event rates taken during the July 2015 and August 2016 runs at Clatterbridge.*

Run	Rate kHz	χ^2_{red} window	Number of waveforms Total	Accepted	Fraction retained %	Purity %	False positive %
093 (July 2015)	200–300	0–100	20480	17991	87.9	99	1.0
050 (August 2016)	250	0–70	184320	151994	82.5	100	1.0
053 (August 2016)	500	0–70	273408	96254	35.2	100	2.0

Based on the location of where there is a sharp drop-off in values in the χ^2_{red} distributions found from using both the fit outlined earlier in Equation 15 consisting of two straight lines and an exponential and the newer fit outlined in Equation 16 to the 250 kHz data obtained during the August 2016 test beam run (see Fig. 45), an acceptance limit for χ^2_{red} of ∼70 was chosen for filtering.

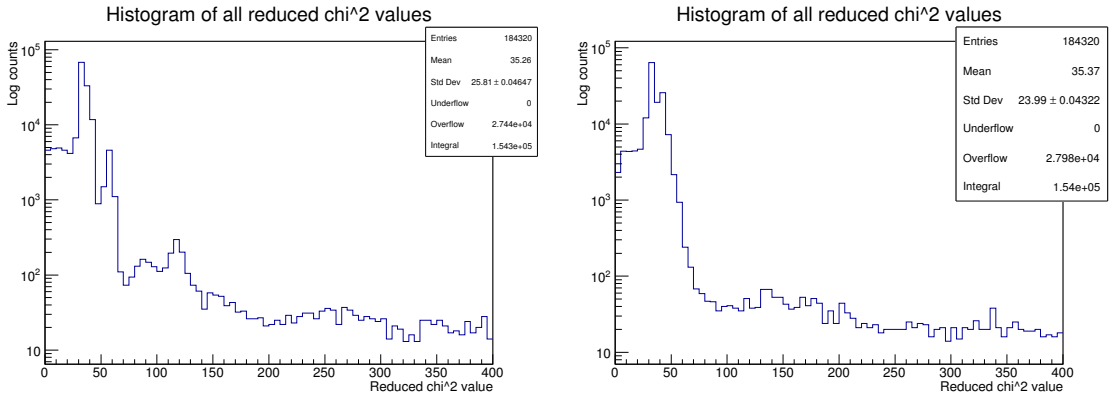

(a) **(b)**

Figure 45: *Reduced χ^2 distributions of the fit using **(a)** two straight lines and an exponential and **(b)** a straight line, Gaussian and biphasic exponential to the 250 kHz rate data.*

For the 250 kHz data set from the August 2016 the fraction retained was found to be 82.5%. A purity of 100% and false-positive count of 1 was found for the first 100 eye-scanned waveforms.

Waveforms which returned values which passed the χ^2 cut after fitting with the Gaussian-Exponential piecewise function were integrated over the long gate by summation of all the ADC input bin values of the waveforms between the start and end of the long gate. These integrated ADC values were passed to a histogram to generate the pulse-integrated ADC spectrum absent of entries which failed to pass the χ^2 cut.

The energy resolution from fitting the resulting ADC spectrum with the Landau-Gaussian convolution with mirrored Landau tail was found to be 2.337±0.024% FWHM without a filter applied and $2.315 \pm 0.025\%$ FWHM with a $0 \leq \chi^2_{\text{red}} < 70$ acceptance filter utilising the two straight lines and an exponential for a χ^2 fit applied (Fig. 46a). For an acceptance filter with the same cut utilising the Gaussian and biphasic exponential fit, the energy resolution was found to be $2.312 \pm 0.026\%$ FWHM (Fig. 46b). While both filters result in a very slight reduction in the energy resolution both are within errors and cannot be said to have significantly improved.

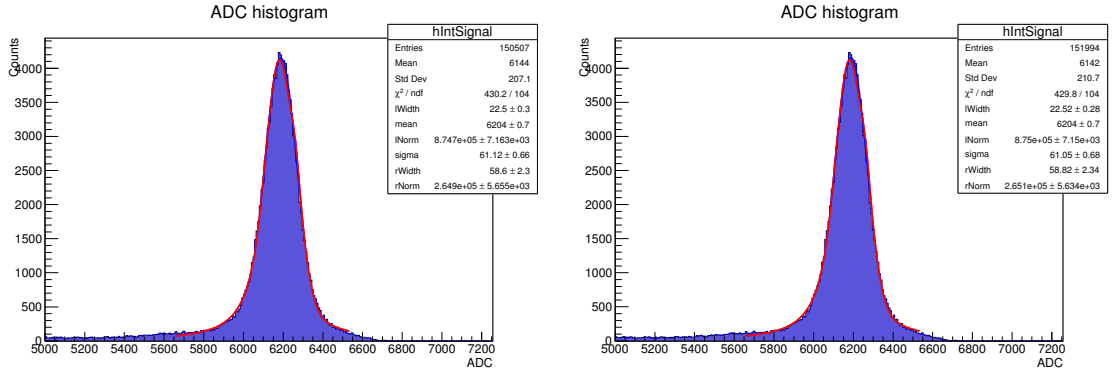

(a) **(b)**

Figure 46: *Landau-Gaussian convolution fit over a -4.5σ to 3σ range to the 250 kHz rate data after filtering with the fit using* ***(a)*** *two straight lines and an exponential and* ***(b)*** *a Gaussian with a biphasic exponential for a $\chi^2_{red} < 70$ cut.*

Pre-filtering, two small bumps at higher reconstructed ADC values to the main peak — at approximately 11000 and just over 12000 ADC as seen in the blue histogram data in Fig. 48a and Fig. 48b — are present. Assuming the protons arrive at roughly equal intervals this means a 250 kHz proton rate will give one proton every 40 ns. As the integration gate was set to 150 ns it is probable that pulse pile-up will have occurred. With the larger bump at $\sim$ 12000 ADC being approximately double the mean value of the main peak, which was found to be 6204 ADC from fitting (Fig. 45a and Fig. 46b), this is likely to be as a result of pulse pile-up within the integration gate. The smaller bump at $\sim$ 11000 may be a result of the integration gate clipping the start of another pulse in the next RF bucket. Due to time constraints, investigation of the subsets of individual waveforms contained within both of the bumps could not be completed to confirm this hypothesis. Post-filtering with

both fits, which can be seen as the red histogram data in the aforementioned figures, both of the bumps are absent.

An acceptance limit for χ^2_{red} of $\sim$70 was chosen for filtering for the higher rate 500 kHz dataset from the August 2016 run, again based on the location of where there is a distinct and sharp drop-off in values in the χ^2_{red} distributions found from using the newer fit outlined in Equation 16 (see Fig. 49). For the 500 kHz dataset, the unfiltered reconstructed waveform histogram (seen in Fig. 52d) appears to be very broad. A look at the peak ADC input value distributions (Fig. 47) for the 500 kHz dataset shows large variation ranging from $\sim$ 180 to $\sim$ 500 mV in the peak values. As the energy of the protons exiting the cyclotron should be almost monoenergetic and such a large variation in proton energy would be detected during clinical beam calibration, this is highly unlikely to be as a result of the beam itself.

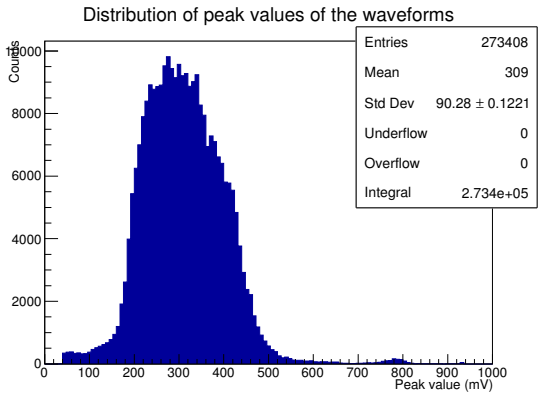

Figure 47: *Distribution of peak ADC input values of the pulses for the 500 kHz dataset from the August 2016 run.*

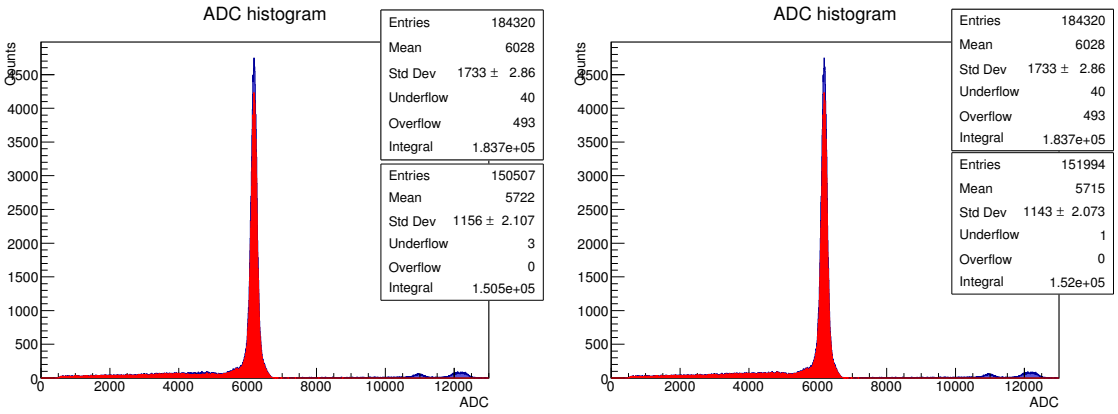

(a) **(b)**

Figure 48: *Comparison of reconstructed ADC waveform histograms before (blue histogram)and after (red histogram) filtering at $\chi^2_{red} < 70$ using the **(a)** two straight lines and an exponential filter and **(b)** a straight line, Gaussian and biphasic exponential filter to the 250 kHz rate data.*

For the 500 kHz dataset, an energy resolution could not be found via fitting the unfiltered ADC spectrum (seen in Fig. 52d) as the fitting using the Landau-

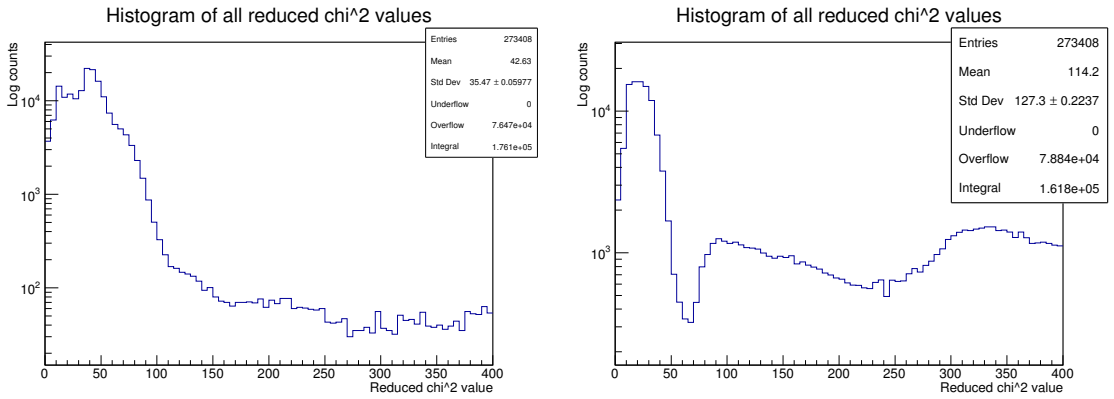

(a) **(b)**

Figure 49: *Reduced χ^2 distributions of the fit using* ***(a)*** *two straight lines and an exponential and* ***(b)*** *a straight line, Gaussian and biphasic exponential to the* 500 *kHz rate data.*

Gaussian convolution with mirrored Landau tail was unsuccessful due to the fit being unable to converge on a value. Post-filtering with a $0 \leq \chi^2_{\text{red}} < 70$ acceptance filter utilising the two straight lines and an exponential for a χ^2 fit applied, some of the higher ADC pulses — particularly those at higher ADC than the main peak — and some of the lower ADC pulses are removed (Fig. 52b) and an energy resolution of $25.339 \pm 0.218\%$ FWHM was found (Fig. 50a). For an acceptance filter with the same cut utilising the Gaussian and biphasic exponential fit, a much sharper cut-off at higher ADC edge of the peak resulted, in addition to a reduction in the waveforms at the lower ADC edge of the peak (Fig. 52c). While the overall peak appears narrower (Fig. 52f), an energy resolution could not be found as the Landau-Gaussian convolution with mirrored Landau tail fit (Fig. 50b) was unsuccessful in returning a sensible value. In particular, the lower ADC edge of the peak remains noticeably broader compared to the usual ADC histogram shape. As the rejection criteria is based upon the χ^2 result, it is possible that waveforms contaminated with smaller pulses, or waveforms that were smaller to begin with but also contaminated, returned a low χ^2 comparative in value to uncontaminated but larger pulses and passed the χ^2 cut (see Figure 51). Due to lack of time, investigation of individual waveforms in this lower ADC subset was not completed.

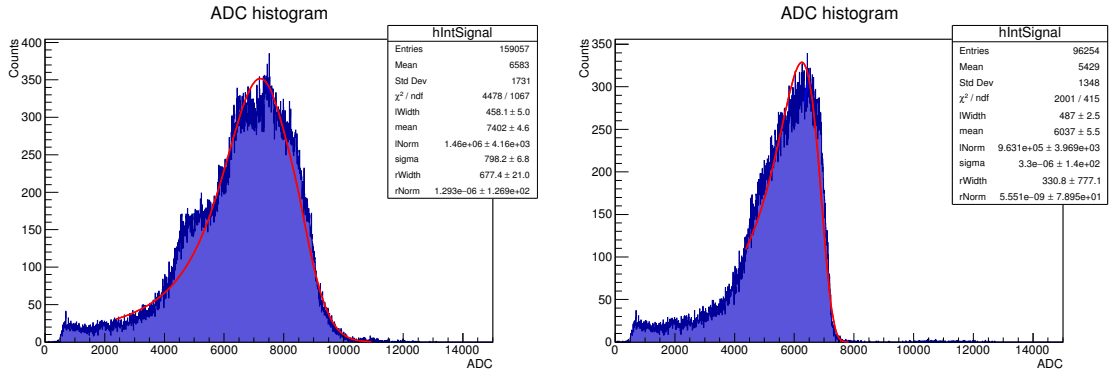

(a) **(b)**

Figure 50: *Landau-Gaussian convolution fit over a -4.5σ to 3σ range to the 500 kHz rate data after filtering with the fit using* ***(a)*** *two straight line and exponential and* ***(b)*** *Gaussian with biphasic exponential for a $\chi^2_{red} < 70$ cut.*

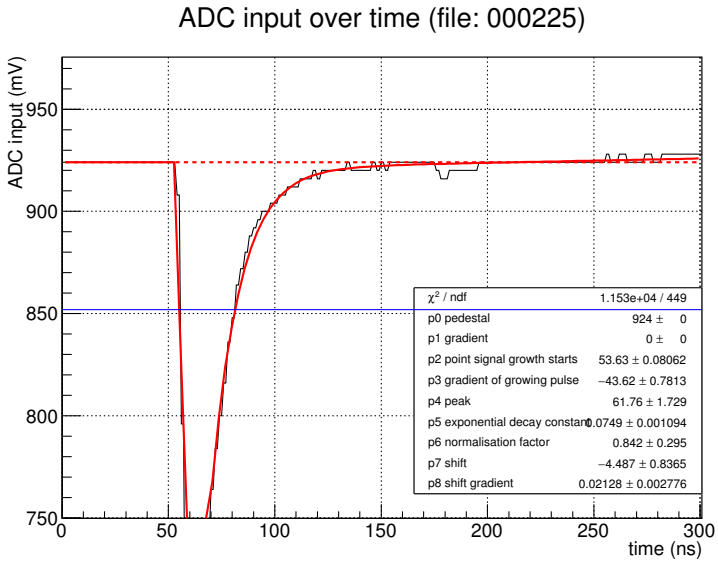

Figure 51: *Close-up of a waveform from the 500 kHz dataset with the piecewise Gaussian and biphasic exponential fit applied, which was sorted as a 'good' waveform, having passed the $0 \leq \chi^2_{red} < 70$ acceptance filter. Aside from the main pulse at 60 ns, a second smaller peak of ~ 10 mV can be seen at ~ 180 ns.*

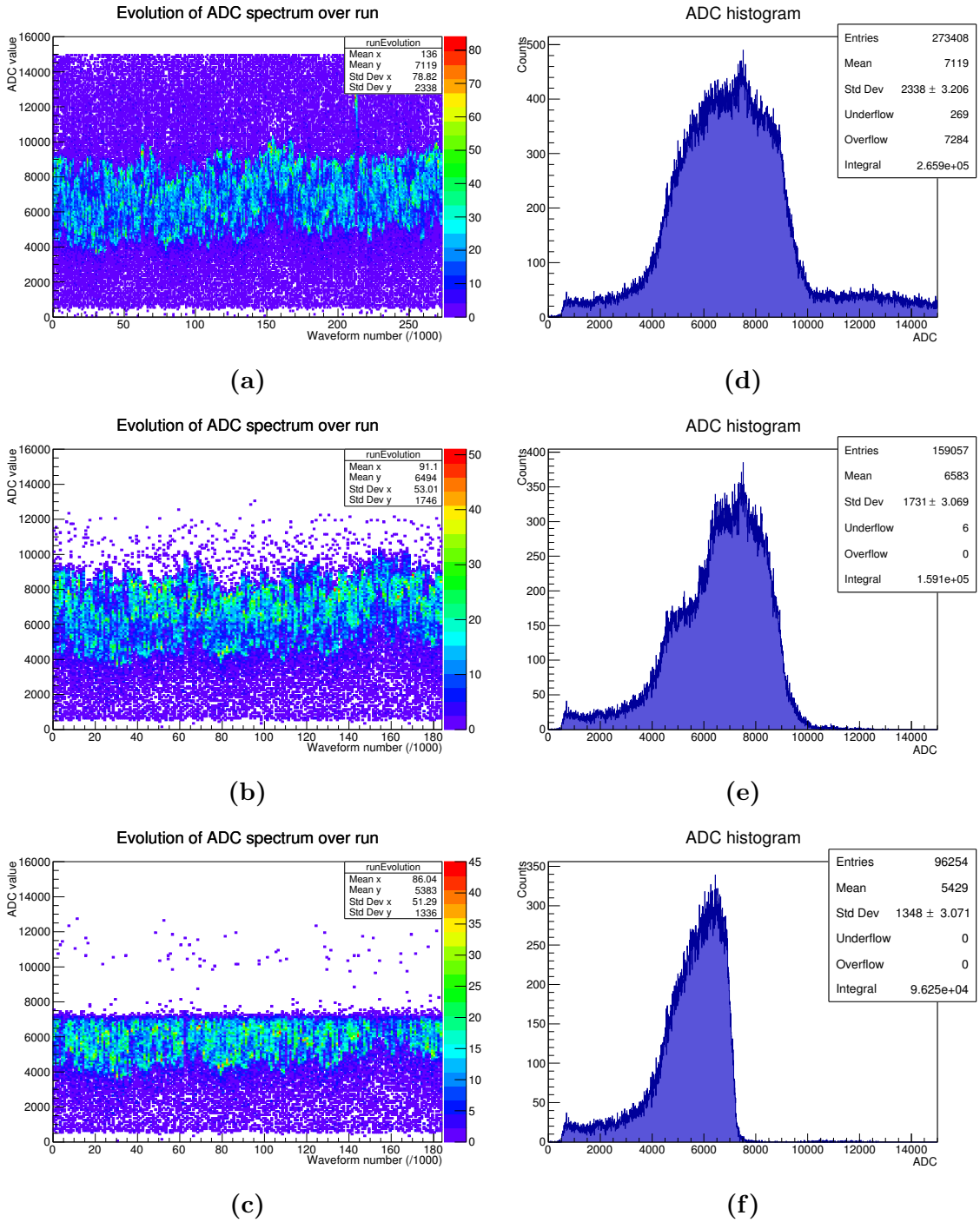

Figure 52: *Evolution of ADC values per 1000 pulses for the 500 kHz waveform dataset obtained during the August 2016 run at Clatterbridge with* ***(a)*** *no filter applied,* ***(b)*** *the cut for all fits returning $\chi^2 > 100$ using 2 straight lines and an exponential filter,* ***(c)*** *the cut for all fits returning $\chi^2 > 70$ using the Gaussian and biphasic exponential filter. The corresponding reconstructed ADC histograms using the aforementioned respective filters can be seen in* ***(d)****,* ***(e)*** *and* ***(f)****.*

10 Discussion

While the EJ-Block energy resolution showed a definite improvement in energy resolution with proton energy, and the fit initially appears to conform well to the data, this is a potentially unphysical empirical fit wherein one cannot necessarily apply a physical interpretation to the parameter values that are returned. Finding a more physically motivated fit to the data would be beneficial such that the fit could be utilised to extrapolate expected energy resolutions of the detectors at higher energies, and for any further insight to be gained into the physical parameters affecting the relationship between the detector's energy resolution and the proton energy.

During analysis of the waveform data, pulses were occasionally encountered which, though still possessing the characteristic exponential rise and fall components of the proton pulses, were much smaller than the majority of the population. It was suggested that the small pulses in the waveforms may have come from protons that did not deposit all their energy before escaping the scintillator or other secondary particles, such as neutrons, that may have been generated along the beamline by the protons.

One avenue of investigation is via simulation of the Clatterbridge beamline and the traversal of the 60 MeV protons through its components. Preliminary investigations [81] using GEANT4 simulations shows protons with kinetic energies down to < 10 MeV exiting the nozzle, suggesting that at least some of the smaller pulses were low energy protons produced by the beamline. An increase in neutron flux has been found to occur at several locations, particularly at the brass stopper and collimators. Though neutron flux was shown to be low past the nozzle, some low energy neutrons (all < 40 MeV with vast majority < 10 MeV) were produced within a simulated water volume detector placed just past the nozzle [82]. As such, the possibility that some of the smaller waveform pulses may be secondary production neutrons cannot be discounted at this stage.

Distinguishing between the pulses produced by protons and neutrons for the purposes of reducing neutron pulse contamination from datasets could potentially be achieved via pulse-shape discrimination, particularly characterisation of the fast and slow decay constants for the pulse-shape fitting, a method that has been used to distinguish between neutron and photon pulses [83].

During analysis of several waveform datasets, particularly those at high rates (Figures 35b and 40), the energy of the spectra appeared to shift over the course of a run. As it is highly unlikely that the energy of the proton beam itself was changing, it is much more likely an effect of the detector. It was hypothesized that this was potentially a result of the frequency dependant gain of the PMTs in use, wherein at higher proton rates the increased light levels from the scintillator resulted in the increase of the anode current caused by the electron cascade — required to be much less than that of the DC current running through the resistor chain for linearity — to levels too high relative to the DC current. In an attempt to circumvent this effect

and keep the PMTs operating in their working regimes, new custom designed PMTs were ordered from Hamamatsu, where the base signal was collected from the 4th and 5th dynodes. As testing with these custom PMTs remains ongoing, no confirmation as to whether the shifts in the energy spectra over time were caused by this issue or resolved can be made at present.

Suggestions that the shift in energy spectra may have come about in line with changes in proton flux could potentially be investigated by plotting of the ADC count against time as opposed to a subset of waveforms, e.g. per 1000 pulses as in Figure 35. As the waveform datasets obtained to date have not contained global timestamps, merely local timestamps within each waveform, retrospective analysis in this manner cannot be performed on data collected thus far. Recording waveform data embedded with global timestamps would be a simple method of investigation, providing no software or hardware limitations with regards to the current digitiser setup.

11 Conclusions

An additional margin of error is added to proton therapy treatment plans to account for the uncertainty resulting from conversion errors introduced when X-ray CT scans are converted into a format to be used for proton treatment plans. This leads to more healthy tissue being irradiated. Eliminating such conversion errors via the use of pCT requires the knowledge of both the path of the proton and the residual energy to accurately determine the range of protons in the patient. The energy resolution of a calorimeter to determine the residual energy should have less spread than caused by the energy straggling which is typically $1\%\,\sigma$. For viable clinical throughput, such a detector needs to process the high number of events required for patient image reconstruction at an extremely high rate, where pulse pile-up events become significant. Pulse-shape analysis was performed on the proton pulse waveforms and a χ^2 filter was constructed as a means to reduce pile-up events in recorded waveform data, with the aim of increasing detector resolution from a software point-of-view. Investigation into the use of waveform discrimination via pulse-shape analysis finds that while pulse pile-up events can be rejected it has not led to a significant improvement in energy resolution.

While the required energy resolution of $< 1\%\,\sigma$ was achieved for the EJ-Block module for the ADC spectrum recorded directly from the digitiser with protons at 60 MeV, it was not achieved from the energy spectra reconstructed from waveform data taken with either the Hex module or the EJ-Block module either before or after filtering for pile-up was applied.

For the enhanced cuboid module an energy resolution of $2.337 \pm 0.024\%$ FWHM ($\sigma = 0.99\%$) was obtained without a filter applied and $2.312 \pm 0.026\%$ FWHM ($\sigma = 0.98\%$) obtained after filtering. While values both before and after filtering achieve the $< 1\%$ required energy resolution requirement for a calorimeter to be used in clinical computed tomography, there is no significant improvement post filtering. It is still a potentially viable method for excluding pile-up contaminated data if it could be made to run on-the-fly without significantly compromising evaluation speed.

Several waveform datasets obtained displayed shifts in the mean energy of the reconstructed energy spectrum over the duration of a run. This is unlikely to be as a result of a change in energy of the actual beam, however a potential cause is the frequency-dependant nature of the gain of the PMT, but this is an area still under investigation.

References

[1] W. Parker and H. Patrocinio, *Radiation Oncology Physics: A Handbook for Teachers and Students*. IAEA, 2005, ch. Chapter 7: Clinical Treatment Planning in External Photon Beam Radiotherapy, pp. 219–272. http://www-pub.iaea.org/books/IAEABooks/7086/Radiation-Oncology-Physics

[2] U. Weber and G. Kraft, "Comparison of carbon ions versus protons," *The Cancer Journal*, vol. 15, no. 4, 2009. http://journals.lww.com/journalppo/Fulltext/2009/08000/Comparison_of_Carbon_Ions_Versus_Protons.10.aspx

[3] H. Paganetti, *Proton Therapy Physics*, ser. Series in Medical Physics and Biomedical Engineering. CRC Press, 2011, ch. Characteristics of Clinical Proton Beams, pp. 103–124. https://books.google.co.uk/books?id=IGPRBQAAQBAJ

[4] E. B. Podgoršak, *Radiation Oncology Physics: A Handbook for Teachers and Students*. IAEA, 2005, ch. Chapter 1: Basic Radiation Physics, pp. 1–43. http://www-pub.iaea.org/books/IAEABooks/7086/Radiation-Oncology-Physics

[5] M. Berger, J. Coursey, and J. Chang. Stopping-power and range tables for electrons, protons, and helium ions. Accessed 16 September 2015. http://www.nist.gov/pml/data/star/

[6] S. Kane, *Introduction to Physics in Modern Medicine, Second Edition*. CRC Press, 2009, ch. Chapter 6: Diagnostic Xrays and CT scans, pp. 187–258. https://books.google.co.uk/books?id=iD_OBQAAQBAJ

[7] C.-W. Cheng *et al.*, "Comparison of tissue characterization curves for different CT scanners: implication in proton therapy treatment planning," *Translational Cancer Research*, vol. 1, no. 4, 2013. https://dx.doi.org/10.3978/j.issn.2218-676X.2012.11.05

[8] N. R. C. U. C. on Glossary of Terms in Nuclear Science and Technology, *A Glossary of Terms in Nuclear Science and Technology*, ser. ASME standard. American Society of Mechanical Engineers, 1957. https://books.google.co.uk/books?id=-zgrAAAAYAAJ

[9] R. Wisniewski. (2014, July) Prototype CT scanner could improve targeting accuracy in proton therapy treatment. http://www.quantumdiaries.org/2014/07/21/prototype-ct-scanner-could-improve-targeting-accuracy-in-proton-therapy-treatment/

[10] S. A. Uzunyan *et al.*, "A New Proton CT Scanner," *ArXiv e-prints*, Aug. 2014.

[11] C. Amsler *et al.*, "Plastic scintillation spectrometry," *Physics Letters*, vol. B667, no. 1, p. 10, 2008.

[12] Hamamatsu. Hamamatsu - photocathode technology. [Accessed 16 September 2015]. http://www.hamamatsu.com/jp/en/technology/innovation/photocathode/index.html

[13] ELJEN. ELJEN Technology - EJ-200. [Accessed 16 September 2015]. http://www.eljentechnology.com/index.php/component/content/article/31-general/48-ej-200mat

[14] NHS Foundation Trust. Cyclotron. [Accessed 15 February 2016]. http://www.clatterbridgecc.nhs.uk/professionals/physics-department/cyclotron

[15] D. E. Bonnett, A. Kacperek, M. A. Sheen, R. Goodall, and T. E. Saxton, "The 62 MeV proton beam for the treatment of ocular melanoma at Clatterbridge." *Br J Radiol*, vol. 66, no. 790, pp. 907–914, Oct 1993. https://dx.doi.org/10.1259/0007-1285-66-790-907

[16] ELJEN. ELJEN Technology - EJ-204. [Accessed 7 February 2016]. http://www.eljentechnology.com/index.php/products/plastic-scintillators/60-product-template

[17] National Cancer Institute. Types of treatment. Accessed 7 September 2015. http://www.cancer.gov/about-cancer/treatment/types

[18] D. R. Beil and L. M. Wein, "Analysis and comparison of multimodal cancer treatments." *IMA J Math Appl Med Biol*, vol. 18, no. 4, pp. 343–376, Dec 2001.

[19] Y. A. Luqmani, "Mechanisms of drug resistance in cancer chemotherapy," *Medical Principles and Practice*, vol. 14(suppl 1), no. Suppl. 1, pp. 35–48, 2005. http://www.karger.com/DOI/10.1159/000086183

[20] M. Goitein and M. Jermann, "The relative costs of proton and x-ray radiation therapy," *Clinical Oncology*, vol. 15, no. 1, pp. S37–S50, February 2003. http://dx.doi.org/10.1053/clon.2002.0174

[21] R. Baskar, K. A. Lee, R. Yeo, and K.-W. Yeoh, "Cancer and radiation therapy: Current advances and future directions," *Int J Med Sci*, vol. 9, no. 3, pp. 193–199, 2012. http://dx.doi.org/10.7150/ijms.3635

[22] G. C. Barnett *et al.*, "Normal tissue reactions to radiotherapy: towards tailoring treatment dose by genotype," *Nat Rev Cancer*, vol. 9, no. 2, pp. 134–142, 02 2009.
http://dx.doi.org/10.1038/nrc2587

[23] U. Ringborg *et al.*, "The Swedish Council on Technology Assessment in Health Care (SBU) Systematic Overview of Radiotherapy for Cancer including a Prospective Survey of Radiotherapy Practice in Sweden 2001–Summary and Conclusions," *Acta Oncologica*, vol. 42, no. 5-6, pp. 357–365, 2003.
http://www.tandfonline.com/doi/abs/10.1080/02841860310010826

[24] National Cancer Institute. NCI Dictionary of Cancer Terms: carcinogenesis. Accessed 16 February 2016.
http://www.cancer.gov/publications/dictionaries/cancer-terms?CdrID=46487

[25] M. Goitein, *Radiation Oncology: A Physicist's-Eye View*. New York, NY: Springer New York, 2008, ch. Proton Therapy in Water, pp. 211–245.
http://dx.doi.org/10.1007/978-0-387-72645-8_10

[26] P. Mayles, A. Nahum, and J. Rosenwald, *Handbook of Radiotherapy Physics: Theory and Practice*. CRC Press, 2007, pp. 451–482.
https://books.google.co.uk/books?id=v68J1dgCEn8C

[27] A. Gardner, M. A. Bagshaw, V. Page, and C. J. Karzmark, "Tumor localization, dosimetry, simulation and treatment procedures in radiotherapy: The isocentric technique," *American Journal of Roentgenology*, vol. 114, no. 1, pp. 163–171, 2016/02/16 2012.
http://dx.doi.org/10.2214/ajr.114.1.163

[28] I. C. on Radiation Units & Measurements, "Prescribing, recording and reporting photon beam therapy — report 50," Report, 1993.
http://www.icru.org/home/reports/prescribing-recording-and-reporting-photon-beam-therapy-report-50

[29] I. C. on Radiation Units & Measurements, "Prescribing, recording and reporting photon beam therapy — report 62," Report, 2001.
http://www.icru.org/home/reports/prescribing-recording-and-reporting-photon-beam-therapy-report-62

[30] A. K. Berthelsen *et al.*, "What's new in target volume definition for radiologists in ICRU Report 71? How can the ICRU volume definitions be integrated in clinical practice?" *Cancer Imaging*, vol. 7, pp. 104–116, 2007.
http://dx.doi.org/10.1102/1470-7330.2007.0013

[31] PTCOG. Particle therapy facilities in operation: Information about technical equipment and patient statistics (last update: 31-august-2015). [Accessed 14 September 2015].
http://www.ptcog.ch/index.php/facilities-in-operation

[32] W. Bragg M.A. and R. Kleeman, "LXXIV. On the ionization curves of radium," *Philosophical Magazine Series 6*, vol. 8, no. 48, pp. 726–738, 1904.
http://dx.doi.org/10.1080/14786440409463246

[33] T. Bortfeld, H. Paganetti, and H. Kooy, "Moat6b01: Proton beam radiotherapy — the state of the art," *Medical Physics*, vol. 32, no. 6, pp. 2048–2049, 2005.
http://dx.doi.org/10.1118/1.1999671

[34] R. R. Wilson, "Radiological use of fast protons," *Radiology*, vol. 47, no. 5, pp. 487–491, 1946, pMID: 20274616.
http://dx.doi.org/10.1148/47.5.487

[35] A. Niemierko, M. Urie, and M. Goitein, "Optimization of 3D radiation therapy with both physical and biological end points and constraints." *Int J Radiat Oncol Biol Phys*, vol. 23, no. 1, pp. 99–108, 1992.
http://dx.doi.org/10.1016/0360-3016(92)90548-V

[36] O. Jakel, D. Schulz-Ertner, C. P. Karger, A. Nikoghosyan, and J. Debus, "Heavy ion therapy: status and perspectives." *Technol Cancer Res Treat*, vol. 2, no. 5, pp. 377–387, Oct 2003.
https://www.ncbi.nlm.nih.gov/pubmed/14529303

[37] H. Suit *et al.*, "Proton vs carbon ion beams in the definitive radiation treatment of cancer patients," *Radiotherapy and Oncology*, vol. 95, no. 1, pp. 3 – 22, 2010.
http://dx.doi.org/10.1016/j.radonc.2010.01.015

[38] G. A. Johansen and P. Jackson, *Radioisotope Gauges for Industrial Process Measurements*. John Wiley & Sons, Ltd, 2005, ch. Appendix B: Formulae Derivation and Examples, pp. 271–283.
http://dx.doi.org/10.1002/0470021098.app2

[39] A. Akara, H. Baltas, U. Çevikc, F. Korkmazb, and N. T. Okumuşoğlu, "Measurement of attenuation coefficients for bone, muscle, fat and water at 140, 364 and 662 keV γ-ray energies," *Journal of Quantitative Spectroscopy & Radiative Transfer*, vol. 106, pp. 203–211, 2006.
http://dx.doi.org/10.1016/j.jqsrt.2006.02.007

[40] E. B. Podgoršak, *Radiation Physics for Medical Physicists*. Berlin, Heidelberg: Springer Berlin Heidelberg, 2010, ch. Introduction to Modern Physics, pp.

1–75.
http://dx.doi.org/10.1007/978-3-642-00875-7_1

[41] G. Molière, "Theorie der Streuung schneller geladener Teilchen I. Einzelstreuung am abgeschirmten Coulomb-Feld," *Zeitschrift Naturforschung Teil A*, vol. 2, pp. 133–145, Mar. 1947.
http://dx.doi.org/10.1515/zna-1947-0302

[42] H. A. Bethe, "Molière's theory of multiple scattering," *Phys. Rev.*, vol. 89, pp. 1256–1266, Mar 1953.
http://dx.doi.org/10.1103/PhysRev.89.1256

[43] J. Rice, *Mathematical Statistics and Data Analysis*, ser. Advanced series. Cengage Learning, 2006, no. p. 3, ch. Limit Theorems, pp. 177–191.
https://books.google.co.uk/books?id=EKA-yeX2GVgC

[44] Y.-S. Tsai, "Pair production and bremsstrahlung of charged leptons," *Rev. Mod. Phys.*, vol. 46, pp. 815–851, Oct 1974.
https://link.aps.org/doi/10.1103/RevModPhys.46.815

[45] C. Patrignani and Particle Data Group, "Review of Particle Physics," *Chinese Physics C*, vol. 40, no. 10, p. 100001, Oct. 2016.

[46] K. Peach, P. Wilson, and B. Jones, "Accelerator science in medical physics," *The British Journal of Radiology*, vol. 84, no. special_issue_1, pp. S4–S10, 2011, pMID: 22374548.
http://dx.doi.org/10.1259/bjr/16022594

[47] J. Beringer *et al.*, "Review of particle physics*," *Phys. Rev. D*, vol. 86, p. 010001, Jul 2012.
http://dx.doi.org/10.1103/PhysRevD.86.010001

[48] F. A. J. Mettler *et al.*, "Medical radiation exposure in the U.S in 2006: Preliminary results," *Health Physics*, vol. 95, no. 5, pp. 502–507, November 2008.
https://dx.doi.org/10.1097/01.HP.0000326333.42287.a2

[49] S. Penfold, R. Schulte, Y. Censor, V. Bashkirov, and A. Rosenfeld, "Characteristics of proton CT images reconstructed with filtered backprojection and iterative projection algorithms," in *Nuclear Science Symposium Conference Record (NSS/MIC), 2009 IEEE*, Oct 2009, pp. 4176–4180.
https://dx.doi.org/10.1109/NSSMIC.2009.5402282

[50] V. Sipala *et al.*, "A proton computed tomography system for medical applications," *Journal of Instrumentation*, vol. 8, no. 02, p. C02021, 2013.
https://dx.doi.org/10.1088/1748-0221/8/02/C02021

[51] H. Paganetti, "Range uncertainties in proton therapy and the role of Monte Carlo simulations," *Phys Med Biol*, vol. 57, no. 11, pp. 99–117, Jun 2012.

[52] M. F. Moyers, M. Sardesai, S. Sun, and D. W. Miller, "Ion stopping powers and CT numbers," *Med Dosim*, vol. 35, no. 3, pp. 179–194, 2010.

[53] G. Coutrakon *et al.*, "Design and construction of the 1st proton CT scanner," in *AIP Conference Proceedings*, vol. 1525, no. 1, 2013, pp. 327–331. http://dx.doi.org/10.1063/1.4802343

[54] A. M. Cormack and A. M. Koehler, "Quantitative proton tomography: preliminary experiments," *Physics in Medicine and Biology*, vol. 21, pp. 560–569, Jul. 1976. http://adsabs.harvard.edu/abs/1976PMB....21..560C

[55] K. M. Hanson *et al.*, "Computed tomography using proton energy loss." *Phys Med Biol*, vol. 26, no. 6, pp. 965–983, Nov 1981. https://dx.doi.org/10.1088/0031-9155/26/6/001

[56] R. W. Schulte *et al.*, "Density resolution of proton computed tomography." *Med Phys*, vol. 32, no. 4, pp. 1035–1046, Apr 2005. https://dx.doi.org/10.1118/1.1884906

[57] H.-W. Sadrozinski *et al.*, "Operation of the preclinical head scanner for proton CT," *Nuclear Instruments and Methods in Physics Research Section A: Accelerators, Spectrometers, Detectors and Associated Equipment*, pp. –, 2016. http://dx.doi.org/10.1016/j.nima.2016.02.001

[58] T. Li *et al.*, "Reconstruction for proton computed tomography by tracing proton trajectories: a monte carlo study." *Med Phys*, vol. 33, no. 3, pp. 699–706, Mar 2006. https://dx.doi.org/10.1118%2F1.2171507

[59] K. Y. Kim *et al.*, *World Congress on Medical Physics and Biomedical Engineering, September 7 - 12, 2009, Munich, Germany: Vol. 25/3 Radiation Protection and Dosimetry, Biological Effects of Radiation*. Berlin, Heidelberg: Springer Berlin Heidelberg, 2009, ch. Identification of Neutron-Induced Isotopes in Varian LINAC System, pp. 616–619. http://dx.doi.org/10.1007/978-3-642-03902-7_177

[60] R. Wigmans, *Calorimetry: Energy Measurement in Particle Physics*, ser. International Series of Monographs on Physics. Oxford University Press, 2000, pp. 225–231.

[61] G. Knoll, *Radiation Detection and Measurement*. John Wiley & Sons, 2010. https://books.google.co.uk/books?id=4vTJ7UDel5IC

[62] F. Scholze *et al.*, *Handbook of Practical X-Ray Fluorescence Analysis*. Berlin, Heidelberg: Springer Berlin Heidelberg, 2006, ch. X-Ray Detectors and XRF Detection Channels, pp. 199–308.
http://dx.doi.org/10.1007/978-3-540-36722-2_4

[63] J. Verplancke, P. F. Fettweis, R. Venkataraman, B. M. Young, and H. Schwenn, "Chapter 5 - semiconductor detectors," in *Handbook of Radioactivity Analysis (Third Edition)*, 3rd ed., M. F. L'Annunziata, Ed. Amsterdam: Academic Press, 2012, pp. 299 – 362.
http://dx.doi.org/10.1016/B978-0-12-384873-4.00005-0

[64] L. Marcu and E. Bezak, *Biomedical Physics in Radiotherapy for Cancer*, 1st ed. Springer-Verlag London, 2012, p. 19.

[65] W. Rall, *The atomic nucleus*. McGraw Hill Book Company, Inc., New York, 1956, vol. 2, no. 3.
http://dx.doi.org/10.1002/aic.690020327

[66] F. H. Attix, *Introduction to Radiological Physics and Radiation Dosimetry*. Wiley-VCH Verlag GmbH, 2007, ch. Charged-Particle Interactions in Matter, pp. 160–202.
http://dx.doi.org/10.1002/9783527617135.ch8

[67] M. Weber, "Scintillation: mechanisms and new crystals," *Nuclear Instruments and Methods in Physics Research Section A: Accelerators, Spectrometers, Detectors and Associated Equipment*, vol. 527, no. 1–2, pp. 9 – 14, 2004, proceedings of the 2nd International Conference on Imaging Technologies in Biomedical Sciences.
http://dx.doi.org/10.1016/j.nima.2004.03.009

[68] G. Laustriat, "The luminescence decay of organic scintillators," *Molecular Crystals*, vol. 4, no. 1-4, pp. 127–145, 1968.
http://dx.doi.org/10.1080/15421406808082905

[69] J. E. Turner, *Atoms, Radiation, and Radiation Protection*, 3rd ed. Wiley-VCH Verlag GmbH & Co. KGaA, 2007, ch. Chapter 10. Methods of Radiation Detection, pp. 241–301.
http://dx.doi.org/10.1002/9783527616978.ch10

[70] C. Burt, "Plastic scintillation spectrometry," Ph.D. dissertation, Faculty of Engineering, Science & Mathematics, University of Southampton, 2009.

[71] R. Wigmans, *Calorimetry: Energy Measurement in Particle Physics*, ser. International Series of Monographs on Physics. Oxford University Press, 2000, no. 144–145.

https://global.oup.com/academic/product/calorimetry-9780198502968?cc=gb&lang=en&#

[72] A. Basharina-Freshville and the SuperNEMO Collaboration, "Calorimeter R&D for the superNEMO double beta decay experiment," *Journal of Physics: Conference Series*, vol. 293, no. 1, p. 012037, 2011. http://dx.doi.org/10.1088/1742-6596/293/1/012037

[73] A. C. Guyton, *Textbook of Medical Physiology*, 8th ed. W.B. Saunders Co., 1991, p. 274.

[74] T. Buzug, *Computed Tomography: From Photon Statistics to Modern Cone-Beam CT*. Berlin, Heidelberg: Springer Berlin Heidelberg, 2008, ch. Fundamentals of X-ray Physics, pp. 15–73. http://dx.doi.org/10.1007/978-3-540-39408-2_2

[75] J. A. Clarke *et al.*, "Assessing the suitability of a medical cyclotron as an injector for an energy upgrade," in *Proc. 6th European Particle Accelerator Conference*, vol. 4, 1998, pp. 2374–2376. https://www.researchgate.net/publication/235765395_Assessing_the_Suitability_of_a_Medical_Cyclotron_as_an_Injector_for_an_Energy_Upgrade

[76] NHS Foundation Trust, "Cyclotron," The Clatterbrige Cancer Centre, NHS, March 1 2014, [Accessed 16 September 2015]. http://www.clatterbridgecc.nhs.uk/application/files/8814/3498/7113/ProtonBeamTherapytotheEyeV3.0.pdf

[77] N. Kanematsu, Y. Koba, and R. Ogata, "Evaluation of plastic materials for range shifting, range compensation, and solid-phantom dosimetry in carbon-ion radiotherapy." *Med Phys*, vol. 40, no. 4, p. 041724, Apr 2013. https://dx.doi.org/10.1118/1.4795338

[78] A. M. Koehler, R. J. Schneider, and J. M. Sisterson, "Flattening of proton dose distributions for large-field radiotherapy." *Med Phys*, vol. 4, no. 4, pp. 297–301, Jul-Aug 1977. https://dx.doi.org/10.1118/1.594317

[79] D. E. Bonnett, A. Kacperek, and M. A. Sheen, "Characteristics of a 62 MeV proton therapy beam," in *Proc. EPAC1990*, June 12–16 1990, p. 1787. https://accelconf.web.cern.ch/accelconf/e90/PDF/EPAC1990_1787.PDF

[80] S. Webb, *The Physics of Three Dimensional Radiation Therapy: Conformal Radiotherapy, Radiosurgery and Treatment Planning*, ser. Series in Medical Physics and Biomedical Engineering. CRC Press, 1993, ch. 4.3 Range

modulation and production of large-area beams, pp. 186–197. https://books.google.co.uk/books?id=2kKStkqe4UUC

[81] M. Hentz. Kinetic energy of the proton beam. [Accessed 2 October 2017]. http://www.hep.ucl.ac.uk/pbt/wiki/Clatterbridge#Kinetic_energy_of_the_proton_beam

[82] M. Hentz. Neutron flux along beamline and kinetic energy. [Accessed 2 October 2017]. http://www.hep.ucl.ac.uk/pbt/wiki/Clatterbridge#Neutron_flux_along_beamline_and_kinetic_energy

[83] S. D. Clarke, S. A. Pozzi, M. A. Norsworthy, and E. King, "Pulse shape fitting for pulse shape discrimination and light output applications," in *57th Annual Meeting of the Institute of Nuclear Materials Management (INMM 2016)*, vol. 3, 2016, pp. 2267–2271.